

VODKA: Complex molecular gas dynamics in a kpc-separation $z = 2.17$ dual quasar with ALMA

YUZO ISHIKAWA ^{1,2}, NADIA L. ZAKAMSKA ¹, YU-CHING CHEN ¹, ANDREY VAYNER ^{1,3}, YUE SHEN ⁴,
XIN LIU ^{4,5,6}, HSIANG-CHIH HWANG ⁷, SWETHA SANKAR ¹ AND ARRAN C. GROSS ⁴

¹Department of Physics and Astronomy, Johns Hopkins University, Baltimore, MD 21218, USA

²MIT Kavli Institute for Astrophysics and Space Research, Massachusetts Institute of Technology, Cambridge, MA 02139, USA

³IPAC, California Institute of Technology, 1200 E. California Boulevard, Pasadena, CA 91125, USA

⁴Department of Astronomy, University of Illinois at Urbana-Champaign, Urbana, IL 61801, USA

⁵National Center for Supercomputing Applications, University of Illinois at Urbana-Champaign, Urbana, IL 61801, USA

⁶Center for Artificial Intelligence Innovation, University of Illinois at Urbana-Champaign, 1205 West Clark Street, Urbana, IL 61801, USA

⁷School of Natural Sciences, Institute for Advanced Study, 1 Einstein Drive, Princeton, NJ 08540, USA

ABSTRACT

In galaxy mergers, dual quasars — two actively accreting supermassive black holes (SMBHs) — provide a unique opportunity to study the interplay between galaxy dynamics and quasar activity. However, very little is known about their molecular gas, which fuels star formation and quasar activity. In this study, we map the kinematics of the cold molecular gas in J0749+2255, a 3.8 kpc separation dual quasar at $z = 2.17$ using the Atacama Large Millimeter Array (ALMA) Band 4. We detect CO(4–3) $\lambda 650\mu\text{m}$, which shows remarkably complex morphological and kinematic structures. While the integrated CO map suggested a lens-like ring, this feature disappears with kinematic decomposition. The kinematic analysis with ALMA resolves the ambiguities introduced by previous observations, further supporting the dual quasar interpretation of J0749+2255. We find two kinematically distinct molecular gas components: spatially extended, yet dynamically complex slow-moving gas (FWHM $\sim 130\text{ km s}^{-1}$), and a compact, blueshifted, fast-moving, turbulent gas (FWHM $\sim 300\text{ km s}^{-1}$). The disturbed kinematics, likely driven by the merger, show hints of rotation but no molecular outflows, suggesting circumnuclear flows. We estimate a large molecular gas reservoir ($M_{\text{H}_2} \sim 10^{10} M_{\odot}$), yet the starburst activity appears to exceed the available fuel. We detect an extended continuum in excess at rest-frame 455 GHz. The kinematic complexity of CO implicates the connection of mergers on the starburst and quasar activity in J0749+2255, yet whether J0749+2255 represents the dual quasar population remains unclear. Targeted kinematic studies of larger dual quasar samples will be essential to disentangling the nature of dual quasars.

Keywords: Double quasars (406) – Supermassive black holes (1663) – Active galactic nuclei (16) – Galaxy mergers (608) – Molecular gas (1073) – Submillimeter astronomy (1647)

1. INTRODUCTION

Over the past several decades, there has been increasing evidence for the co-evolution of galaxies and the supermassive black holes (SMBHs) they harbor (Silk & Rees 1998; Matteo et al. 2005). Following a merger of two galaxies, the two central SMBHs may spiral into the center through dynamical friction and interaction with the gas and stars to form a bound binary (e.g. Begelman

et al. 1980; Milosavljević & Merritt 2001; Blaes et al. 2002; Yu 2002). When two SMBHs in merging galaxies are actively accreting during inspiral, they can be observed as a dual quasar (active galactic nuclei; AGN). Although there is some evidence that quasar activity may be enhanced in dual SMBHs due to gas flows during a merger (e.g. Begelman et al. 1980; Hopkins & Hernquist 2009) the mechanisms for quasar triggering remain poorly understood and hotly debated (e.g. Mechtley et al. 2016). Gas infall may be triggered by merger-induced tidal torques or even secular accretion. Since dual quasars are found in galaxy mergers, studying dual

quasars may help unravel the poorly understood connection between SMBH fueling, quasar triggering, and galactic dynamics.

Whatever the fueling mechanism, quasar activity requires an abundant supply of cold, dense gas transported to the circumnuclear regions (Heckman & Best 2014). Dense molecular gas reservoirs provide fuel for both star formation (Carilli & Walter 2013) and quasar activity. This means that the fate of the molecular gas phase is a key link in understanding the relationship between quasars and their host galaxies. Typically, the second most abundant molecule, carbon monoxide (CO), is used as a tracer of the molecular gas, which is dominated by molecular hydrogen (H_2). Unlike H_2 , CO has a much lower excitation energy, requiring gas temperatures above ~ 5 K, which makes it easier to observe (Carilli & Walter 2013). Observations of the cold molecular gas phase at high sensitivity and angular resolution have been enabled by observatories such as ALMA.

Over the past several years, extensive studies have explored the molecular properties of quasar host galaxies. Past studies of quasar hosts have revealed diverse and, at times, contradictory molecular gas properties. Kinematic measurements revealed compact hosts with rotating disks and irregular morphologies with disturbed kinematics (e.g. Díaz-Santos et al. 2016; Banerji et al. 2017; Brusa et al. 2018; Feruglio et al. 2018; Bischetti et al. 2021). Intense star formation rates (SFRs), up to several $\gtrsim 1,000 M_\odot \text{ yr}^{-1}$, have been observed in some host galaxies (Maiolino et al. 2012; Duras et al. 2017; Fan et al. 2019; Nguyen et al. 2020). Some studies find that quasar hosts exhibit higher star formation efficiency than galaxies without a quasar (e.g. Bischetti et al. 2017), but others did not find any significant differences (e.g. Kirkpatrick et al. 2019; Valentino et al. 2021). Quasar hosts have been found to be CO/molecular gas depleted (e.g. Kakkad et al. 2017; Brusa et al. 2018; Bischetti et al. 2021; Vayner et al. 2021; Bertola et al. 2024), raising the question whether quasar host galaxies lie on or off the “main sequence” of star formation (e.g. Xie et al. 2021). It is unclear if these variations are due to quasar feedback in the form of molecular outflows or due to galaxy interactions (e.g. Kakkad et al. 2017; Trakhtenbrot et al. 2017; Bischetti et al. 2018; Brusa et al. 2018; Fan et al. 2019; Herrera-Camus et al. 2019; Vayner et al. 2021).

Despite progress in studying the molecular gas properties of quasar host galaxies, many questions remain unanswered — especially for dual quasars, whose overall properties are still poorly understood. The challenges stem from difficulties in identifying reliable candidates and disentangling the quasar and host galaxy

light. However, recent advances in spatially resolved imaging and spectroscopy have begun to shed light on their rest-frame ultraviolet and optical properties. Some reveal complex merger activity (Treister et al. 2018; Koss et al. 2018; Tubín et al. 2021), some reveal intense star formation with disk-dominated host galaxies (Chen et al. 2023b, 2024; Ishikawa et al. 2024), and some reside in complex environments (Perna et al. 2023). Limited studies of the molecular gas have detected CO and [C II]158 μm emission (e.g. Treister et al. 2018; Koss et al. 2023; Tang et al. 2024). Some studies inferred large molecular gas reservoirs exceeding $10^9 M_\odot$ (Treister et al. 2018; Tang et al. 2024). Complex molecular gas dynamics, including velocity gradients, tidal tails, and even gas bridges that connect the two quasars have been detected (Izumi et al. 2024), possibly linked to the ongoing merger activity (Treister et al. 2018; Koss et al. 2023). Quasar feedback has been suggested in some dual quasar systems (Tang et al. 2024; Izumi et al. 2024), yet their prevalence remains unclear.

In this paper, we obtain and analyze spatially resolved ALMA observations of the molecular gas traced with CO in SDSSJ074229.96+225511.7 (J0749+2255, henceforth), a dual quasar at $z = 2.17$. Although the CO(1–0) transition is ideal for tracing the total molecular gas, we choose the CO(4–3) $\lambda 650\mu\text{m}$ transition, the best observable line during Cycle 9. This paper aims to probe the impact of galaxy mergers on the host galaxies and their central SMBHs. In Section 2 we summarize the known properties of J0749+2255 and outline the new ALMA observation and data reduction. Throughout this paper, we refer to both dual AGNs and dual quasars as “dual quasars” for simplicity. In Section 3 we present the spectral analyses. We discuss the interpretation of the data in Section 4, and conclude in Section 5. We adopt the Λ CDM cosmology with $h = 0.7$, $\Omega_M = 0.3$, and $\Omega_\Lambda = 0.7$.

2. OBSERVATIONS AND DATA REDUCTION

2.1. Summary of J0749+2255

In the last decade, techniques have been significantly refined to search for close quasar pairs systematically. The advent of large-scale imaging surveys such as Subaru/HSC (Aihara et al. 2018) and *Gaia* (Prusti et al. 2016) allows for a systematic search for close quasar pairs. In particular, two methods using *Gaia* have pioneered the discovery of sub-arcsec pairs: Varstrometry for off-nucleus and dual subkiloparsec AGN (VODKA) and *Gaia* Multi Peak (GMP), which capitalize on the superb precision astrometry and excellent point-spread function of *Gaia* (Shen et al. 2019; Hwang et al. 2020; Mannucci et al. 2022). The method of interest in this

paper is VODKA, which searches for light centroid jitters caused by the asynchronous stochastic variability of unresolved quasar pairs (Shen et al. 2019; Hwang et al. 2020). These *Gaia*-based methods have been successful in identifying dual quasar candidates with $< 1''$ or kpc-scale separations. Follow-up studies have confirmed some of these candidates as bona fide dual quasars, lensed quasars, and star-quasar superpositions (e.g. Chen et al. 2022; Ciurlo et al. 2023; Scialpi et al. 2024).

J0749+2255 is a VODKA-selected dual quasar at $z = 2.17$. It was initially spectroscopically identified as a Type 1 quasar by the Sloan Digital Sky Survey (SDSS; Schneider et al. 2010). Follow-up Hubble Space Telescope (HST) and VLA-A (6 GHz and 15 GHz) observations revealed two point-like cores separated by $\sim 0.5''$, corresponding to a physical separation of ~ 3.8 kpc, (Shen et al. 2021; Chen et al. 2022, 2023a). The brighter quasar is located to the southwest (J0749+2255-SW, henceforth) and the fainter quasar is located to the northeast (J0749+2255-NE, henceforth). Chen et al. (2023b) outlined the first series of follow-up observations to confirm the nature of the J0749+2255. Spatially-resolved slit-spectroscopy with Gemini/GMOS+GNIRS revealed two distinct quasar spectra. Furthermore, detailed point-spread-function (PSF) modeling of the HST images hinted at extended tidal features that are likely part of an ongoing merger.

Recently, spatially resolved spectroscopy with the James Webb Space Telescope (JWST) detected extended ionized optical and molecular infrared gas associated with the host galaxy using NIRSpec (Ishikawa et al. 2024) and MIRI (Chen et al. 2024). The JWST observations revealed three key results. First, J0749+2255 is hosted by a powerful starburst galaxy with an SFR exceeding $1,000 M_{\odot} \text{ yr}^{-1}$, based on the ionized H α (Ishikawa et al. 2024) and molecular PAH $3.3 \mu\text{m}$ (Chen et al. 2024) emission lines. The optical line ratio diagnostics indicate that these star-forming regions are concentrated close to the two quasars (Ishikawa et al. 2024). Second, the spatially-resolved kinematic analysis of the emission lines suggests the presence of a large rotating gas with a symmetric blue-/redshifted velocity gradient spanning 10 kpc in diameter (Ishikawa et al. 2024). This suggests J0749+2255 is a dual quasar system either hosted by a single galaxy or a merger with complex kinematics.

Third, an unexpected result is that the two quasars have remarkably similar, yet subtly different, spectra and black hole properties, M_{BH} and luminosity (Ishikawa et al. 2024). The natural explanation of the apparent quasar similarity is gravitational lensing in-

stead of a physical dual quasar pair. Although lens modeling of the HST images (Chen et al. 2023b) and JWST kinematic analysis of the two quasars and the extended ionized gas (Ishikawa et al. 2024) argued against the lensing scenario, JWST's improved aperture spectroscopy resurfaced the lensing hypothesis. Interestingly, this strange scenario of similar dual quasars hosted by a single galaxy is predicted by numerical simulations (e.g. Dadiani et al. 2024). Thus, distinguishing between a dual quasar and a lensed double quasar is not clear-cut. In fact, Gross et al. (2023) stresses that exhaustive multi-wavelength analysis is necessary to resolve the ambiguity of close-separation pairs.

Under the lensing hypothesis, reconciling the JWST observations of the extended host galaxy gas with a lensing model remains a key challenge. Specifically, how to split the quasar images while maintaining the kinematics of the large-scale gas disk. To further elucidate the nature of J0749+2255, we use ALMA data to study the cold molecular gas within the framework of two competing interpretations: dual quasar vs. lensed quasar.

2.2. ALMA: Observation and data reduction

The leading goal of the ALMA observation was to detect the CO(4 – 3) and the continuum at the same angular resolution as HST and JWST/NIRSpec. J0749+2255 was observed with ALMA Band 4 in Cycle 9 (2022.1.01427.S; PI: Ishikawa) over three blocks with the C-6 configuration for an effective exposure time of 8,164.74 seconds. This corresponds to an angular resolution of $\sim 0.2''$ (1.66 kpc). The spectral windows were tuned to the redshifted frequency of CO(4–3) at 145.434 GHz and the nearby continuum at 143.538 GHz.

We reduce the ALMA data using the Common Astronomy Software Applications (CASA) version 6.4.1.12 following the procedures in Vayner et al. (2021). The final datacube has a spatial resolution of $0.05''$ per pixel, which corresponds to a plate-scale of ~ 0.5 kpc/pixel.

3. SPECTRAL ANALYSIS

3.1. Continuum emission

In Figure 1 we show the continuum emission centered on the rest-frame frequency of 455.02 GHz ($658 \mu\text{m}$), observed at 143.538 GHz ($2088 \mu\text{m}$) over a bandwidth of 2 GHz. We see two bright clumps that are co-spatial with the known positions of the two quasars and a fainter, extended component stretching asymmetrically to the southwest relative to the two quasars.

We also perform aperture photometry of the continuum centered on each quasar nuclei with aperture radii of $0.15''$ for both J0749+2255-SW and J0749+2255-NE. We compute the monochromatic luminosity co-spatial

Table 1. Summary of ALMA observations. The observed dates include calibration and on-source pointings.

Parameter	Value
Observed Dates	2023-04-22, 2023-05-13, 2023-05-14
Continuum Central Frequency	143.538 GHz
Continuum Beam	$0.292'' \times 0.252''$
Continuum Sensitivity	0.013 mJy/beam over 2.95 MHz
Line Central Frequency	145.434 GHz
Line Beam	$0.296'' \times 0.254''$
Line Sensitivity	0.094 mJy/beam over 15.6275 MHz
Channel Width	32 km s^{-1} per channel

Table 2. Continuum at 143.538 GHz observed frequency. We take $r = 1''$ apertures to calculate the total continuum, which includes the two quasars and the extended component. We also extract the continuum fluxes co-spatial with the two quasars with $r = 0.15''$, which is roughly the half-light radius.

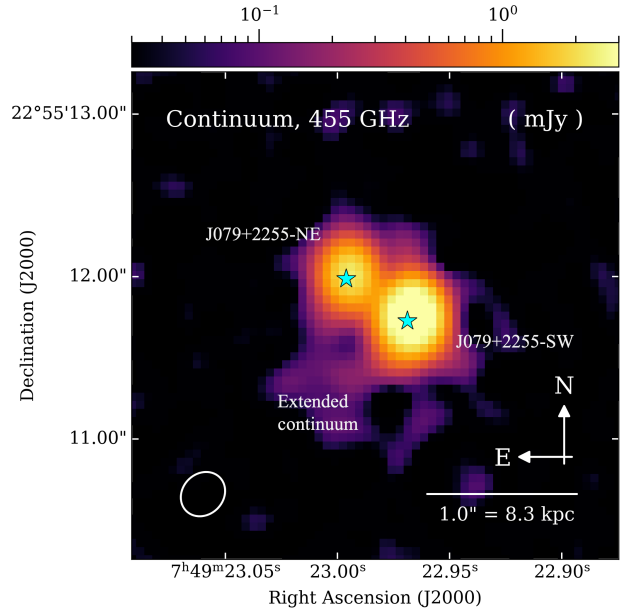
	Total Continuum	J0749+2255-SW	J0749+2255-NE
Flux (Jy)	0.016 ± 0.002	0.0049 ± 0.0005	0.0020 ± 0.0002
νL_ν (erg s $^{-1}$)	$(2.52 \pm 0.35) \times 10^{45}$	$(7.9 \pm 0.9) \times 10^{44}$	$(3.2 \pm 0.5) \times 10^{44}$
νL_ν (L_\odot)	$(6.6 \pm 0.9) \times 10^{11}$	$(2.1 \pm 0.2) \times 10^{10}$	$(8.3 \pm 1.2) \times 10^{10}$

with each quasars, νL_ν , of $(7.9 \pm 0.9) \times 10^{44} \text{ erg s}^{-1}$ and $(3.2 \pm 0.5) \times 10^{44} \text{ erg s}^{-1}$, respectively. The flux ratio of the two quasars' continuum emission ($f_{\text{SW}}/f_{\text{NE}}$) is ~ 2.5 , which differs from the previously measured $f_{\text{SW}}/f_{\text{NE}}$ at rest-frame optical (Chen et al. 2023b; Ishikawa et al. 2024).

The extended continuum component stretches to $1''$ or 8 kpc from the quasars. We integrate over the $r = 1''$ aperture centered at the midpoint of the two quasars to calculate the total continuum flux of $16 \pm 2 \text{ mJy}$, which corresponds to a monochromatic luminosity of $\nu L_\nu = (2.52 \pm 0.35) \times 10^{45} \text{ erg s}^{-1}$ or $(6.6 \pm 0.9) \times 10^{11} L_\odot$. To calculate the uncertainty, we compute the root-mean-square value across a large annular aperture centered on J0749+2255, from $r = 1.75''$ to $20''$. Then we also assume a conservative 10% uncertainty in the ALMA flux calibration. We summarize the measured continuum fluxes and calculated luminosities in Table 2.

3.2. Morphological Analysis of Integrated CO(4-3)

In Figure 2, we show the integrated intensity map and the integrated spectrum of CO(4-3). The CO map is integrated over $\Delta v \approx 800 \text{ km s}^{-1}$. The spectrum is extracted from a circular aperture with a radius $r = 1''$ or 8 kpc centered at the midpoint of the two quasars. The integrated CO map and spectrum reveals morphologically and kinematically complex features. The integrated flux map shows a bright, clumpy, and compact ring-like structure (“CO ring” henceforth) at the center within a $0.3''$ (2.48 kpc) radius, surrounded by a fainter, extended component reaching out to $0.6''$ (4.96 kpc). Assuming this CO ring is an ellipse, the angular size

**Figure 1.** The continuum image centered at the observed frequency 143.538 GHz. The cyan stars indicate the known quasar positions. There are two components to the continuum: the two bright cores corresponding to J0749+2255-SW and J0749+2255-NE and a faint, extended component stretching towards the southeast. We also show the beam size.

of the semi-major and semi-minor axes are $0.3'' \times 0.2''$ ($1.656 \text{ kpc} \times 2.483 \text{ kpc}$) oriented at $\sim 45^\circ$ east of north. The CO ring also appears to connect the two quasars.

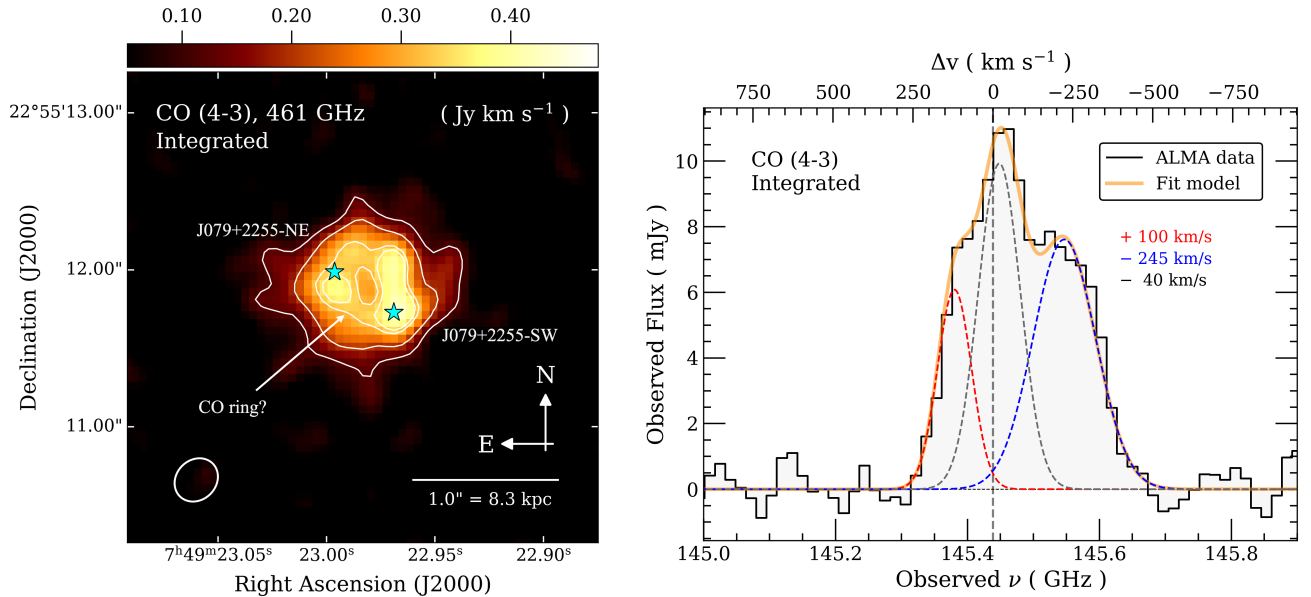


Figure 2. (Left) The continuum-subtracted, velocity-integrated CO(4–3) line intensity over ~ 0.39 GHz (~ 800 km s $^{-1}$). The integrated intensity map is shown in logscale. The cyan stars indicate the known quasar positions. The CO-emitting gas has an extended component out a radius of $\sim 0.6''$ and a bright, compact CO ring concentrated within a radius of $\sim 0.3''$. The white contour lines are set at 0.12, 0.20, 0.32, and 0.35 Jy km s $^{-1}$ to highlight the CO ring structure. The brightest CO clumps are offset from the known quasar positions. We indicate the beam size in the bottom left corner. (Right) The integrated CO(4–3) spectrum, extracted from the $1''$ aperture radius, in the observed frame with the corresponding velocities relative to the rest frame frequency is shown. The integrated spectrum is fit with three Gaussian components, which indicates distinct velocity components: a bright peak centered near z_{sys} , a faint redshifted component with $\Delta v = 100$ km s $^{-1}$, and a broad blueshifted component $\Delta v = -245$ km s $^{-1}$.

Table 3. We summarize the integrated CO(4–3) emission properties (flux, luminosity, and line width). The w_{80} corresponds to the 80th-percentile line width of a non-parametric three Gaussian component fit of the integrated spectrum. The errors represent the 1σ uncertainty.

Parameter	Value
$S_{CO(4-3)}\Delta v$	1.36 ± 0.1 Jy km s $^{-1}$
$L'_{CO(4-3)}$	$(1.94 \pm 0.14) \times 10^{10}$ K km s $^{-1}$ pc 2
$L_{CO(4-3)}$	$(6.07 \pm 0.9) \times 10^7 L_{\odot}$
w_{80}	365 ± 5 km s $^{-1}$

The integrated spectrum reveals a broad and complex emission line profile. We fit the integrated spectrum and find that the best model requires at least three Gaussian components - a bright component blueshifted at -40 km s $^{-1}$, a blueshifted component at -245 km s $^{-1}$, and a fainter redshifted component at $v = 100$ km s $^{-1}$ (Figure 2). These line components have similar velocity dispersions (~ 30 km s $^{-1}$, ~ 20 km s $^{-1}$, and ~ 15 km s $^{-1}$, respectively). The fit slightly improves with an additional Gaussian component, but the fitting parameters become degenerate with one another. To quantify the effective, non-parametric line width, we

quote the effective 80-percentile line width (w_{80} ; Zakamska & Greene 2014) of the integrated CO spectrum. First, we construct the cumulative flux distribution from the best-fit three Gaussian profiles. Then we determine the 10th and 90th percentile velocities of the total flux, v_{10} and v_{90} , where w_{80} is the difference $w_{80} = v_{90} - v_{10}$. For a single Gaussian, $w_{80} = 2.563 \sigma = 1.088$ FWHM. We find widths reaching $w_{80} \approx 350$ km s $^{-1}$, whereas the cold gas in typical massive galaxies has line widths $w_{80} < 200$ km s $^{-1}$ (e.g. He et al. 2023; Rizzo et al. 2023) after converting from the published full-width-at-half-max (FWHM) values. Although luminous quasars are known to have broader molecular line widths (e.g. Bischetti et al. 2021), these are typically associated with fast-moving outflows. These fit results suggest that the integrated CO spectrum captures a kinematically complex emission, which makes it difficult to assess the nature of the target with the integrated spectrum alone. We explore the spatially resolved kinematic analysis in Section 3.3.

Next, we calculate the integrated CO(4–3) luminosity, $L'_{CO(4-3)}$. Based on the line fits, we measure the total line-integrated flux $S_{CO}\Delta v = 1.36 \pm 0.10$ Jy km s $^{-1}$ and convert it to $L'_{CO(4-3)}$ in units of K km s $^{-1}$ pc 2

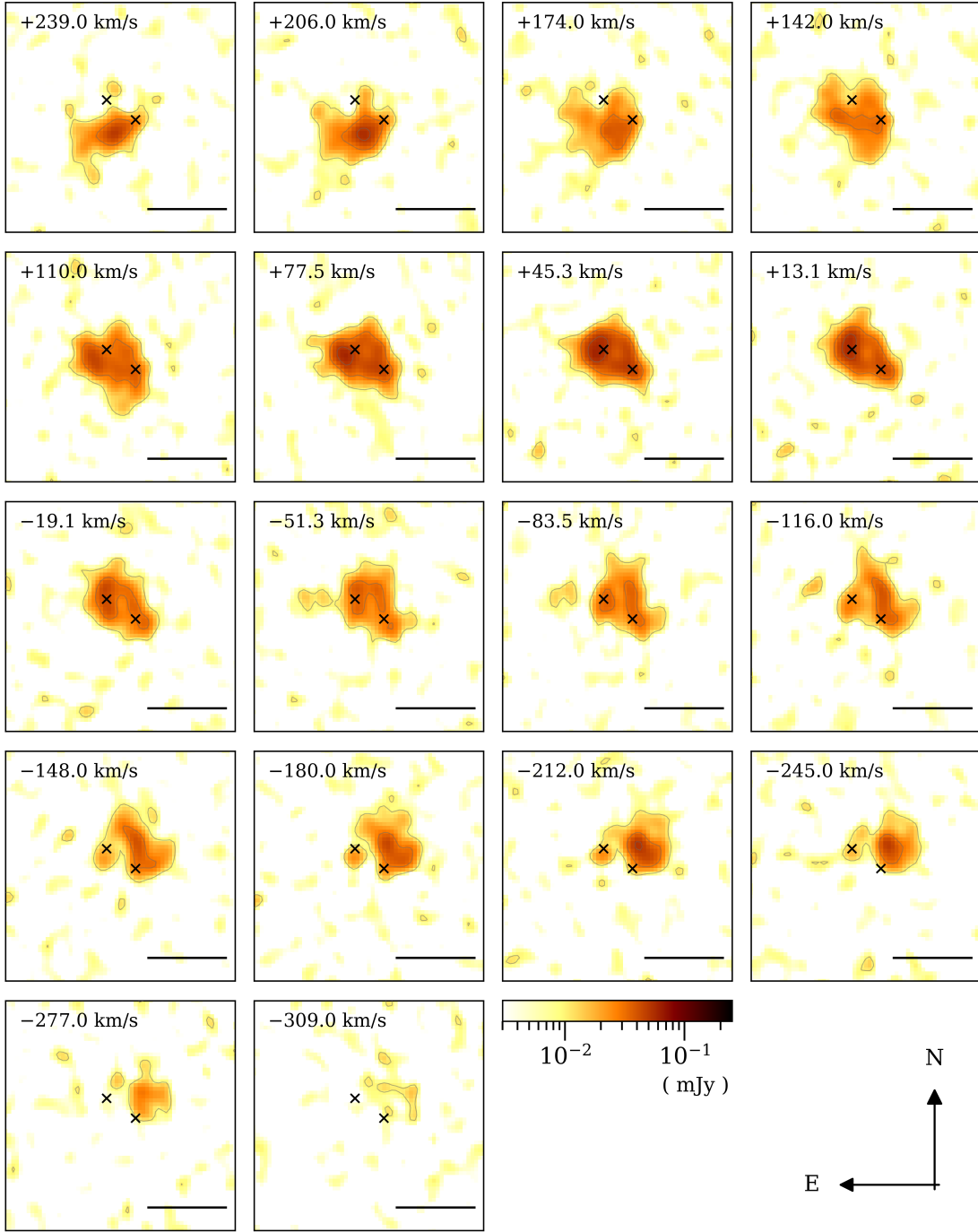


Figure 3. The velocity channel map of the observed CO(4 – 3). We calculate the velocity offset with respect to the rest-frame frequency, assuming $z = 2.169$. Each slice corresponds to the channel width of $\Delta v \sim 32 \text{ km s}^{-1}$. We see different velocity-dependent structures. A clumpy, CO ring is notable around $\Delta v \sim 0 \text{ km s}^{-1}$. Extended blue-/red-shifted features are prominent at $\Delta v \sim \pm 200 \text{ km s}^{-1}$ that appear to be associated with J0749+2255-SW. Each figure has the same scale size as Figures 2. The faint gray contour traces peak channel fluxes at 0.01, 0.03, and 0.05 mJy. All panels share the same log color scale. The solid black scale line indicates $1''$, and the cross-marks indicate the two quasars.

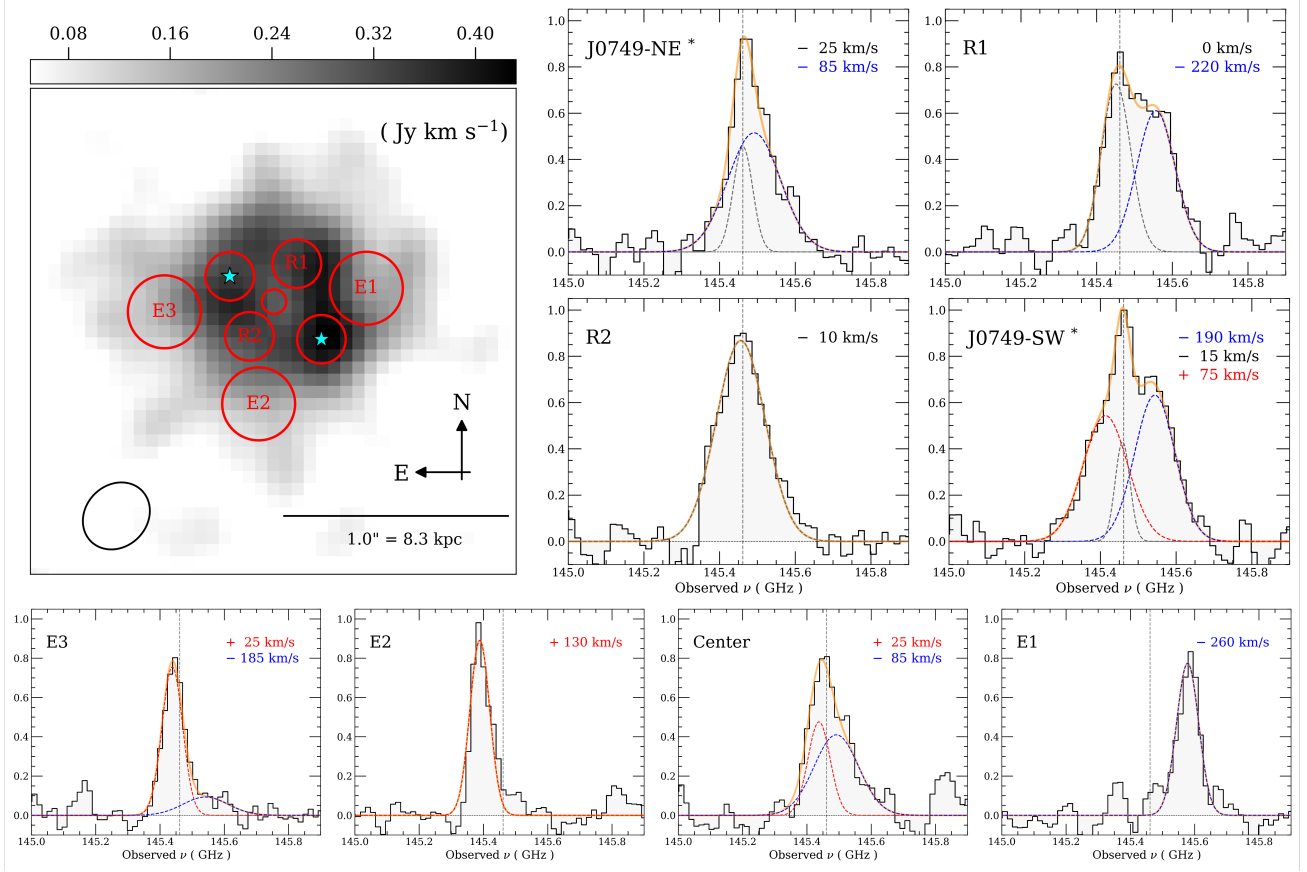


Figure 4. (Top left) Zoom-in of the integrated CO intensity from Figure 2 shown in grayscale, labeled with seven red circular apertures for spectral extraction. (1) the apertures co-spatial with the quasars J0749+2255-SW and J0749+2255-NE, which are indicated with cyan stars; (2) two additional apertures along the inner CO ring, labeled R1 and R2; (3) an aperture at the midpoint of the two quasars and the center of the CO ring; and (4) three apertures from the extended blueshifted and redshifted regions, labeled E1, E2, and E3. The red circle sizes reflect the aperture radii. Apertures SW/NE/R1/R2 were taken at $r = 0.1''$, apertures E1/E2/E3 were taken at $r = 0.15''$, and the unmarked Center aperture was taken at $r = 0.05''$ to avoid overlap. (Top right and bottom row) We show the corresponding aperture spectra. The spectra of J0749+2255-SW, J0749+2255-NE, R1, and R2 are shown to match the relative spatial alignment; E1, E2, and E3 are shown on the bottom row. For each aperture spectra, we show the corresponding best spectral fits. The flux values shown are normalized by the peak flux of J0749+2255-SW to compare the relative fluxes and spectral shapes. We can see significant spectral variations between J0749+2255-SW and J0749+2255-NE.

(Solomon & Vanden Bout 2005; Carilli & Walter 2013):

$$L'_{CO(4-3)} = 3.25 \times 10^7 S_{CO} \Delta v \frac{D_L^2}{(1+z)^3 \nu_{obs}^2} \text{K km s}^{-1} \text{pc}^2, \quad (1)$$

where ν_{obs} is the observed CO(4–3) frequency in GHz, D_L is the luminosity distance in Mpc, and z is the redshift of J0749+2255. We obtain $L'_{CO(4-3)} = (1.94 \pm 0.14) \times 10^{10} \text{K km s}^{-1} \text{pc}^2$, which corresponds to $L_{CO(4-3)} = (6.1 \pm 0.9) \times 10^7 L_\odot$. The flux uncertainty is determined from the line fit errors and is propagated through the $L'_{CO(4-3)}$ calculation. Table 3 summarizes the integrated line values.

3.3. Full spectral fits and kinematic analysis of CO

We first examine the channel map of the ALMA datcube in Figure 3. The velocities of the channels are measured relative to the rest-frame frequency, assuming $z = 2.169$ from (Ishikawa et al. 2024). We see both the extended and compact CO ring structures inferred from the integrated map in Figure 2, but the channel maps indicate a connection between the gas morphology and the velocity shifts. The redshifted region extends to the southeast, and the blueshifted region extends into the northwest. Interestingly, it appears that the CO emission associated with the larger velocity offsets $|\Delta v| > 150 \text{ km s}^{-1}$ is more extended, possibly associated with J0749+2255-SW, whereas the emission with smaller velocity offsets $|\Delta v| < 50 \text{ km s}^{-1}$ is more compact, forming the CO ring that connects both quasars.

Perhaps the most intriguing discovery from the integrated map in Figure 2 is the compact CO ring within about $\pm 50 \text{ km s}^{-1}$ of the systemic redshift. The channel maps suggest a possible velocity differential across the CO ring. For example, the southeast region is brightest in the redshifted gas (up to 100 km s^{-1}) with little blueshifted gas, whereas the northwest region is brighter in the blueshifted gas (up to -150 km s^{-1}) with little redshifted gas.

In Figure 4 we show the aperture spectra extracted from select regions. They are (a) two $r = 0.1''$ apertures co-spatial of the two quasars and the CO ring - J0749+2255-SW and J0749+2255-NE; (b) two additional $r = 0.1''$ apertures along the CO ring - R1 and R2; (c) one $r = 0.05''$ aperture in the middle of the CO ring - Center; and (d) three $r = 0.15''$ apertures that capture the extended CO emission - E1, E2, and E3. Each spectrum is freely fit with up to three Gaussian profiles. First, we compare the aperture spectra taken at J0749+2255-SW and J0749+2255-NE. We find that the CO spectra of J0749+2255-SW and J0749+2255-NE are distinctly different. J0749+2255-SW exhibits broad redshifted and blueshifted components, while J0749+2255-

NE is dominated by a broad blueshifted component. The broad components have $\sigma \sim 120 \pm 10 \text{ km s}^{-1}$. Due to the large aperture extraction, it is unclear whether the broadening is due to fast-moving gas or is a blend of multiple narrow line components. In this step, we assume a single broad line. Interestingly, f_{SW}/f_{NE} of the integrated CO spectrum is ~ 1.2 , which differs from the continuum ratio of ~ 2.5 . We also examine the CO ring with three additional apertures, R1, R2, and Center. There appears to be a narrow component shared in the inner region (J0749+2255-SW, J0749+2255-NE, Center, and R1) with a small, yet varying, velocity offset. The narrow component has widths $\sigma \sim 50 \pm 10 \text{ km s}^{-1}$. R2 does not have an obvious narrow component; however, it is possible that the narrow component and the redshifted, broad components are blended like in the J0749+2255-NE aperture. Center shows a velocity gradient with a narrow redshifted and a broadened blueshifted component. The extended emission at E1, E2, and E3 are narrower at $\sigma \sim 70 \pm 5 \text{ km s}^{-1}$ with some possible blending of the broad components.

To better understand the kinematics of the CO gas, we fit the spectra at each spaxel across the entire field and decompose CO emissions by their different velocity components. For each spaxel element, we extract and fit the CO spectrum with one or two Gaussians with variable σ . An additional third Gaussian component was considered, but was not necessary. We discuss the fit results for the single-component and two-component line fits.

First, we assume the CO emission only requires a single Gaussian component at each spatial element. The corresponding moment maps (integrated line flux F_{int} , velocity shift v_{50} , and line width w_{80}) are shown in Figure 5. We find that the v_{50} map has a similar kinematic morphology to that of the rest-frame optical (i.e. ionized H α) emission lines seen with JWST (Ishikawa et al. 2024). The redshifted region extends to the southeast, and the blueshifted region extends into the northwest. However, unlike the ionized gas velocity map (Ishikawa et al. 2024), the CO velocity map appears more asymmetric and kinematically disturbed. For instance, J0749+2255-NE is surrounded by blueshifted CO, whereas J0749+2255-SW is surrounded by both redshifted and blueshifted gas. Instead of showing the σ maps, we show w_{80} that best identifies regions with complex line profiles, likely requiring additional Gaussian components. The w_{80} map in Figure 5 reveals two zones: one with large w_{80} values that reach 340 to 480 km s^{-1} in dark orange-brown and small w_{80} values with $w_{80} < 150 \text{ km s}^{-1}$ in light yellow-orange. Regions with large w_{80} coincidentally trace the CO ring noted earlier.

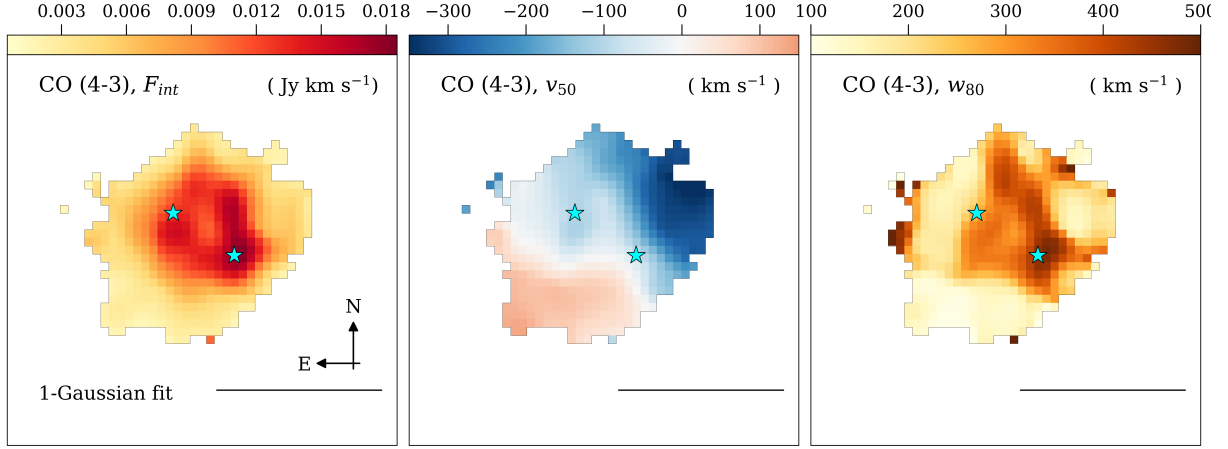


Figure 5. CO(4–3) moment maps assuming single-component Gaussian emission line fits for each spaxel. (Left) F_{int} integrated line intensity; (Center) v_{50} velocity shift, and (Right) w_{80} line width. The CO v_{50} distribution roughly matches the kinematics of the ionized gas as seen with JWST (Ishikawa et al. 2024), although with some differences. The large w_{80} values roughly trace the CO ring seen in Figure 2. The cyan stars indicate the known quasar positions. The solid black scale line indicates $1''$.

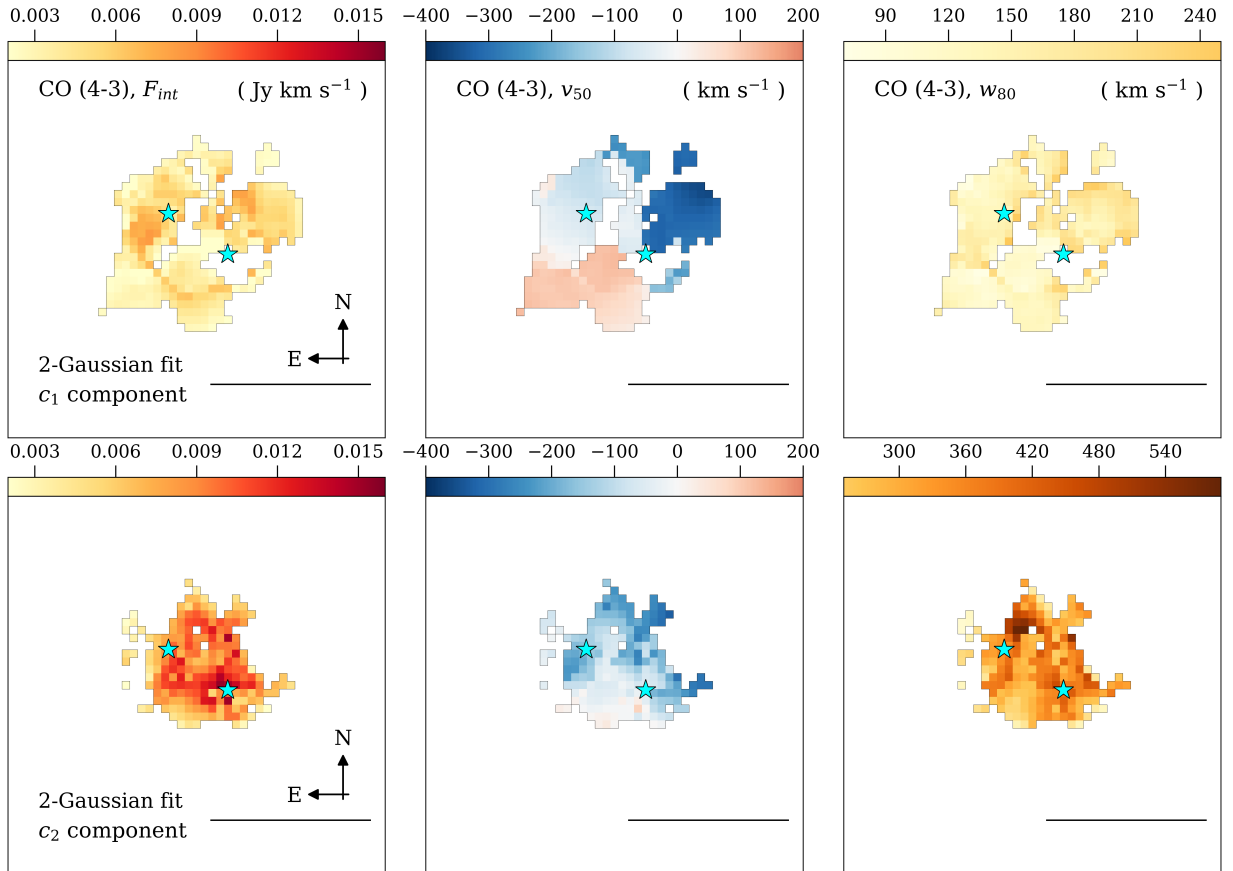


Figure 6. CO(4–3) moment maps for two-component (c_1 , c_2) Gaussian line fits. We sort the components by line widths, in which c_1 has $\sigma < 100 \text{ km s}^{-1}$ and c_2 has $\sigma > 100 \text{ km s}^{-1}$. (Top left/center/right) F_{int} , v_{50} , and w_{80} moment maps for the c_1 component. (Bottom left/center/right) The moment maps for the c_2 component. The spectral decomposition eliminates the large w_{80} CO ring in Figure 5. The cyan stars indicate the known quasar positions. The solid black scale line indicates $1''$.

The measurement of non-uniform distribution and large w_{80} values suggest the need for multiple components, as was demonstrated in Section 3.2. Next, we examine the two-component CO line fit results. In Figure 6, we show the moment maps (F_{int} , v_{50} , and w_{80}) for the two-component (c_1 , c_2) fits. We sort the line components by the velocity dispersion, such that c_1 traces the narrow component ($\sigma < 100 \text{ km s}^{-1}$) with a mean w_{80} of $150 \pm 40 \text{ km s}^{-1}$ and c_2 traces the broader line component ($\sigma > 100 \text{ km s}^{-1}$) with a mean w_{80} of $320 \pm 90 \text{ km s}^{-1}$. Line fits with poor χ^2 goodness-of-fit were excluded.

A different picture of J0749+2255 with kinematically complex CO emerges from the two-component fits. First, distribution of the two gas components is distinct. The c_1 component is spatially extended, whereas the c_2 component is more spatially compact. Second, the two components have different kinematic properties. The c_1 component has complex kinematics with a prominent velocity gradient from $+200 \text{ km s}^{-1}$ to -350 km s^{-1} around J0749+2255-SW, while the c_2 component gas around J0749+2255-NE is mostly blueshifted ranging from -20 to -150 km s^{-1} . The observed v_{50} velocity gradients of c_1 have a similar asymmetric morphology to that of the single-component fit in Figure 5. The c_2 component is almost entirely blueshifted on average by $-120 \pm 90 \text{ km s}^{-1}$. Third, and most importantly, the kinematic decomposition of the CO emission eliminates the CO ring initially identified by the integrated maps in Figures 2 and 5. There is no obvious ring pattern in the integrated flux maps of either component, which may suggest that the CO ring seen in Figure 2 and 5 is not a real physical feature, but rather a visual artifact due to the blending of multiple kinematically independent emission line components. From the two-component fits of the CO emission, it is clear that the CO gas in J0749+2255 is kinematically disturbed.

4. DISCUSSION

Despite the comprehensive and exhaustive multi-wavelength analysis of J0749+2255, differentiating between a physical dual quasar and a pair of lensed images in this target has been challenging. Although this comparison was discussed in detail in Chen et al. (2023b); Ishikawa et al. (2024), we address the lensing hypothesis in the context of the new ALMA results. Then we discuss the implications of the observed CO(4–3) and continuum observations.

4.1. Making the dual quasar case

We summarize all key arguments for/against the lensing and dual quasar hypotheses in Table 4 from this

study and past observations (Shen et al. 2021; Chen et al. 2022, 2023b, 2024; Ishikawa et al. 2024). There are some predictions from the two scenarios that we can compare the data with. In a lensed system, the pair of lensed images of the quasar and its host galaxy would lie along a thin Einstein Ring. Although some spectral variations may be expected, the quasar images would have near-identical spectra with little chromatic dependence. The “smoking-gun” evidence against the lens would be the detection of distinctly different spectra - not explainable by differential reddening - and a velocity offset between the two quasars.

The most surprising result from JWST/NIRSpec aperture spectroscopy was the spectral similarity of the two quasars (Ishikawa et al. 2024). Furthermore, our ALMA observations reveal a compact CO ring that connects the two quasars as shown in Figures 2 and 3. This CO ring morphology is reminiscent of a gravitationally lensed Einstein ring at the angular separation of the two quasars. These two observations are the two leading evidence for lensing.

The key evidence for the dual quasar hypothesis in this study lies in the gas kinematics analysis. First, extended multi-phase gas, reaching beyond the supposed Einstein radius, has been detected with both JWST (Ishikawa et al. 2024) and ALMA (Figures 1-3). This contradicts the expectations of a lensed Einstein ring, which typically has narrow ring widths, in which most of the CO emission should be confined to within the ring. Second, the multi-phase emission corresponding to the two quasars is not identical; we do not see the two mirror images expected from a lensed quasar. JWST detected subtle differences in the optical emission line profiles, including a velocity offset of $\sim 200 \text{ km s}^{-1}$ between the two quasars (Ishikawa et al. 2024). Aperture spectra taken along the CO ring, J0749+2255-SW, and J0749+2255-NE in Figure 4 show significant differences in the spectral profiles, including significant variations in the underlying spectral components. We require different spectral fits for each region: J0749+2255-SW requires three components (two red-/blue-shifted broad components and one narrow component), whereas J0749+2255-NE only requires two blueshifted components (one broad component and one narrow component). Furthermore, ALMA shows that the spatial distribution of the brightest CO clumps does not align with the known quasar positions (contours in Figure 2), which is inconsistent with lensing geometry. While spectral variations in the extended features are not surprising, spectral differences of spectra taken from apertures copatial with the two quasars are more suggestive of different physical properties than lensed images.

Table 4. We summarize all known evidence (morphological, photometric, spectroscopic, and kinematic) for/against the lensing and dual quasar hypotheses. Despite some strong evidence for the lensing hypothesis, they are contradicted by evidence in favor of the dual quasar hypothesis. With the latest addition of ALMA data, we argue that J0749+2255 is indeed a dual quasar.

Evidence	Data	Lensed Quasar	Dual Quasar
Discovery of a quasar pair	a, b	△	△
No detection of foreground lens galaxy	b, d	△	△
Detection of tidal tails	b, d	—	○
Detection of extended multi-phase emission (e.g. H α , PAH, CO)	c, d, e	—	○
λ -dependent $f_{\text{SW}}/f_{\text{NE}}$ differences	b, d, e	△	△
Spectral similarity of nuclear optical	d	○*	△
Spectral differences of nuclear CO(4 – 3)	e	—	○*
Velocity offset ($\sim 200 \text{ km s}^{-1}$, optical) between the quasars	d	—	△
Two SMBH with similar properties (M_{BH} and L_{bol})	d	△	△
H α kinematics suggest rotating gas	d	—	○
Morphologically and kinematically complex CO	e	—	○
Detection of CO ring	e	△*	△
CO ring eliminated with kinematic decomposition	e	—	○*

NOTE— ○ Strong evidence that supports the selected hypothesis. △ Ambiguous evidence that may support either hypothesis or the measurement is uncertain. * Contradictory evidence. ^a Chen et al. (2022); ^b Chen et al. (2023b); ^c Chen et al. (2024); ^d Ishikawa et al. (2024); ^e This ALMA study.

Third, spatially resolved spectroscopy revealed a complex dynamical environment. The kinematic v_{50} maps of both the ionized H α (Ishikawa et al. 2024) and molecular gas (this study) revealed velocity differentials that are suggestive of a large rotating disk or an ongoing merger. Furthermore, the expected parity of the red/blue-shifted regions is not consistent with a lens. If the strongly lensed quasar host galaxy is a disk, then we expect to see a specific kinematic pattern (a mirror pair of red/blue-shifted velocity gradient along the Einstein ring, such as in Riechers et al. 2008 and Liu et al. 2024). Instead, the v_{50} maps in Figures 5 and 6 contradicts this lensing prediction. Most importantly, the kinematic decomposition of the CO emission in Section 3.3 eliminates the CO ring as shown in Figure 6. If the CO ring is an Einstein ring, the kinematic decomposed intensity maps and v_{50} maps should still trace the Einstein ring, which is not what we see. Rather, the CO ring may either represent a real physical phenomenon, such as nuclear rings (e.g. Stuber et al. 2023), or a visual artifact due to the superposition of multiple kinematically independent emission line components.

Other evidence is ambiguous and less robust. In addition to the previously measured wavelength-dependent flux differences (Chen et al. 2023b; Ishikawa et al. 2024), $f_{\text{SW}}/f_{\text{NE}}$ measured with ALMA - the 455 GHz continuum (~ 2.5) and the 650 GHz CO emission (~ 1) - differ. Flux variations likely arise from real physical processes, but they may also result from lensing effects, such as differential reddening (e.g., Sluse et al. 2012), perturbations of the lens mass model (e.g., Stacey & McKean

2018), or misalignment between the lens and source (Agnello et al. 2018). Complex gas kinematics have been seen in some lensed quasars (e.g. Riechers et al. 2008; Stacey & McKean 2018; Lamperti et al. 2021). Also, the non-detection of a foreground lens (Chen et al. 2022, 2024; Ishikawa et al. 2024) does not necessarily confirm the absence of a lens (see Hawkins et al. 1997).

If J0749+2255 is a lensed quasar, then the required lens configuration is two quasar images, surrounded by extended ionized and molecular gases. One possibility is that only the circumnuclear region is lensed and the extended gas appears unlensed because the nuclear gas is depleted. However, this may be an unlikely scenario; either the quasar host galaxy needs to be extremely large in extent or the undetected foreground lens galaxy is extremely massive and compact.

As summarized in Table 4, we learn that ruling out the lensing scenario is not straightforward. However, based on the kinematic analyses, we make the case that J0749+2255 is a dual quasar rather than a lensed double quasar. The challenge with the existing JWST and ALMA data is that we only detect emission lines from the gas associated with the quasar host galaxy. We have yet to detect the stellar continuum, which may better reveal merger signatures. The difficulty may also be characteristic of small-separation dual quasar candidates like J0749+2255. In the following sections, we discuss the implications of the observed molecular gas properties, assuming the dual quasar interpretation.

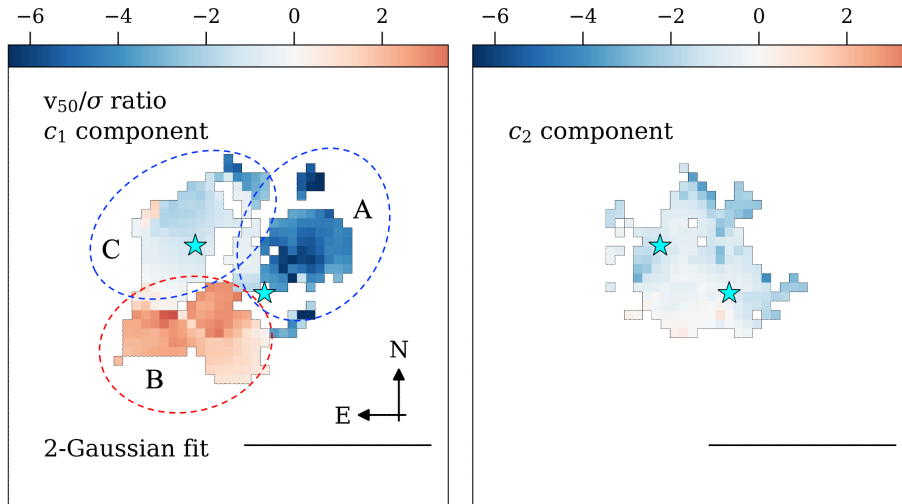


Figure 7. We show the v_{50}/σ ratio of the two-component fits from Figure 6. The red and blue colors indicate redshifted and blueshifted gas, respectively. (Left) The c_1 component, tracing $\sigma \sim 50 \text{ km s}^{-1}$, is kinematically complex gas. It has three distinct kinematic regions: (A) a strongly blueshifted gas with large $v_{50}/\sigma \sim -5$, (B) a moderately redshifted gas with $v_{50}/\sigma \sim 2.5$, and (C) a moderately blueshifted gas with $v_{50}/\sigma \sim -1$. (Right) The c_2 component, tracing $\sigma \sim 150 \text{ km s}^{-1}$, appears to be dispersion dominated, likely due to turbulent fast-moving gas, possibly triggered by the merger dynamics.

4.2. Interpreting the CO kinematics

The emerging picture of J0749+2255 is a dual quasar system with similar SMBH properties embedded in a kinematically complex ionized and molecular gas system. In Section 3.3, we presented the spectral fits of a kinematically disturbed CO. The emission line fits shown in Figures 4 and 6 suggest that J0749+2255 is made up of at least two kinematically different gas components: an extended gas component traced with narrow lines ($w_{80} \sim 150 \text{ km s}^{-1}$) and a compact gas component traced with a broad lines ($w_{80} \sim 320 \text{ km s}^{-1}$).

Based on the line widths of both c_1 and c_2 CO components, it is unlikely that the blue-/red-shifted v_{50} velocity gradient traces biconical quasar-driven molecular outflows. Some quasar-driven molecular outflows are typically characterized by extremely broad lines with FWHM reaching $500 - 1,000 \text{ km s}^{-1}$ (e.g. Stacey et al. 2022). Although the regions around the two quasars show broader line widths reaching $w_{80} \sim 500 \text{ km s}^{-1}$, the majority of the broad line gas is dominated by $w_{80} \lesssim 400 \text{ km s}^{-1}$. Thus, neither component of the two Gaussian fits meets the quasar-outflow criterion. However, we cannot rule out the presence of slow-moving molecular outflows. Interestingly, no ionized gas outflows have been observed with JWST either (Ishikawa et al. 2024), indicating that quasar feedback may not yet be dominant in J0749+2255. If the observed gas kinematics is not well explained by fast-moving quasar outflows, then alternative explanations are merger-driven dynamics or circumnuclear gas flows.

A notable feature of the narrow c_1 component is the velocity gradient in its v_{50} map (Figure 6). This velocity gradient may be evidence for rotation; however, the asymmetry of the v_{50} map complicates this interpretation (Wisnioski et al. 2015). This asymmetry contradicts the analysis of the ionized gas kinematics seen with JWST, which suggested the presence of a large rotating gas disk enveloping both quasars (Ishikawa et al. 2024). Alternatively, the asymmetry of the CO gas kinematics may represent non-circular motions.

In Figure 7 we map the v_{50}/σ ratio corresponding to each of the CO components to characterize the dynamical state of the molecular gas. The v_{50}/σ maps suggest a kinematically disturbed environment with two dynamically distinct systems: a dynamically complex, slow-moving gas and a turbulent, fast-moving gas.

The slow-moving c_1 component appears to be a mix of different dynamical states: a strongly blueshifted gas with large $v_{50}/\sigma \sim -5$ (region A), a moderately redshifted gas with $v_{50}/\sigma \sim 2.5$ (region B), and a moderately blueshifted gas with $v_{50}/\sigma \sim -1$ (region C). The non-uniform distribution of v_{50}/σ indicates that the c_1 component is likely not dominated by large-scale rotation. However, since we detect the positive and negative gradient in v_{50} with relatively large v_{50}/σ centered on J0749+2255-SW (regions A and B), we cannot rule out the presence of a counter-rotating gas, such as a disk host galaxy of J0749+2255-SW. Due to the sharp change in v_{50}/σ along the boundary of regions B and C, these two regions are not likely to represent rota-

tion. Thus, we have two plausible interpretations of the c_1 component: a gas rotation that is kinematically disturbed by the merger, kinematically misaligned and turbulent gas structures, or a combination of both. Numerical simulations also predict that the host galaxies of dual quasars may be disk-dominated (Dadiani et al. 2024). The presence of rotation-like kinematics may indicate that J0749+2255 is still in the early stages of the galaxy merger. On the other hand, the c_2 component has a more uniform distribution of $v_{50}/\sigma \sim -1$, which suggests a dispersion-dominated dynamics. The larger velocity dispersion of the c_2 component also suggests turbulence, possibly heated by a merger, in which this CO gas phase has yet to settle into ordered motion.

The detection of two kinematically complex and distinct CO components suggests the presence of a dual-phase dynamical system that is spatially overlapped. The broadened and blueshifted c_2 gas component suggests the presence of turbulent and fast-moving gas, moving toward the observer. However, it is unclear if the c_1 component traces a rotating gas enveloping both quasars or if it traces two separate galaxies in a merger (i.e. a rotating host galaxy of J0749+2255-SW and a turbulent host galaxy of J0749+2255-NE that is moving towards the observer). Furthermore, it is unclear from the kinematic maps how or if the c_2 gas component is coupled to the two quasars. In Figure 6, there is a small velocity gradient of $\Delta v \sim 120 \text{ km s}^{-1}$ from J0749+2255-NE to J0749+2255-SW, so c_2 gas may trace a tidal bridge connecting J0749+2255-NE and J0749+2255-SW, similar to one observed by Izumi et al. (2024). One hypothesis also presented in Ishikawa et al. (2024) is two merging host galaxies that appear superimposed to the observer (e.g. Tubín et al. 2021; Mazzilli Ciraulo et al. 2021), which results in kinematic ambiguity at the current spectral and spatial resolutions.

Despite the ambiguity in the exact dynamical state of J0749+2255, based on the kinematic analysis of the CO gas it is clear that J0749+2255 is likely in an ongoing galaxy merger that fuels the intense star formation (Chen et al. 2024; Ishikawa et al. 2024) and dual quasar activity. Two possible ways to improve the dynamical assessment in the future is to compare the kinematics of the stellar continuum with the ionized and molecular gas components (Wisnioski et al. 2015) and also to obtain higher spatial resolutions with ALMA.

4.3. Molecular mass estimates

Since CO traces H_2 (Carilli & Walter 2013), we estimate the bulk H_2 mass, M_{H_2} , using the $M_{\text{H}_2} = \alpha_{\text{CO}} L'_{\text{CO}(1-0)}$ relation. Since the CO- M_{H_2} conversion is based on $L'_{\text{CO}(1-0)}$ for the CO(1-0) transition, we

convert from $L'_{\text{CO}(4-3)}$ (Table 3) with the following assumptions. First, we assume that the low-J CO transitions are thermalized and optically thick using the CO excitation correction of $R_{41} = L'_{\text{CO}(4-3)}/L'_{\text{CO}(1-0)} \approx 1$, as in Vayner et al. (2021). Following the Bertola et al. (2024) analysis, we also consider $R_{41} = 0.87$, determined from local quasars (Carilli & Walter 2013), and $R_{41} = 0.37 \pm 0.11$, determined from IR-selected AGNs at cosmic noon (Kirkpatrick et al. 2019). Second, we adopt the CO- H_2 conversion factor of $\alpha_{\text{CO}} = 0.8 \text{ K km s}^{-1} \text{ pc}^2$, typical for local quasars and ULIRGs (Solomon & Vanden Bout 2005; Tacconi et al. 2008), although there are many uncertainties of at least 30% (Bolatto et al. 2013; Papadopoulos et al. 2012) that depend on different conditions in the interstellar medium like gas metallicity to host galaxy's relation to the main-sequence (Elbaz et al. 2007; Noeske et al. 2007; Accurso et al. 2017). We also consider $\alpha_{\text{CO}} = 3.2$ for main-sequence galaxies to place an upper limit on M_{H_2} . Under these assumptions, we calculate M_{H_2} with the following relation:

$$M_{\text{H}_2} = \alpha_{\text{CO}} R_{41}^{-1} L'_{\text{CO}(4-3)}. \quad (2)$$

We summarize the M_{H_2} calculations in Table 5. Our baseline M_{H_2} estimate for $R_{41} = 1$ is $M_{\text{H}_2} = (1.6 \pm 0.1) \times 10^{10} M_{\odot}$. Depending on our choice of R_{41} and α_{CO} , we obtain different estimates for M_{H_2} . Although the choice of R_{41} only results in variations of a factor of few, the choice of α_{CO} results in a variation of about 0.5 dex. The upper limit to M_{H_2} is $M_{\text{H}_2} = (1.6 \pm 0.1) \times 10^{11} M_{\odot}$, based on the $\alpha_{\text{CO}} = 3.2$. The mean value over all of the estimates is $\langle M_{\text{H}_2} \rangle = (6 \pm 5) \times 10^{10} M_{\odot}$.

Based on our initial M_{H_2} calculations, Chen et al. (2024) compared M_{H_2} with the PAH 3.3 μm -based SFR of $\sim 1,000 M_{\odot} \text{ yr}^{-1}$ and found that J0749+2255 is an outlier with an extreme starburst rate that exceeds the available fuel, according to the Kennicutt-Schmidt relation (Kennicutt 1998). The relative agreement with the Kennicutt-Schmidt relation depends strongly on the choice of R_{41} and α_{CO} . For example, if we choose values corresponding to local quasars and dusty starbursts, J0749+2255 deviates strongly from the Kennicutt-Schmidt relation. However, if J0749+2255's host galaxy is a main-sequence galaxy, then the calculated SFR/ M_{H_2} ratio is consistent with the Kennicutt-Schmidt relation. Based on the known star formation and quasar properties of J0749+2255 and the inferred merger activity, it is unlikely that its host galaxy is main-sequence-like.

One explanation of the deviation from the Kennicutt-Schmidt relation is that the merger dynamics help facilitate the rapid conversion of gas to stars, as well as fueling of the two quasars. An alternative interpretation

Table 5. We show the total molecular mass, M_{H_2} , derived from L'_{CO} listed in Table 3. We calculate M_{H_2} using different CO excitation correction from CO(4–3) to CO(1–0), $R_{4,1}$, and different CO-H₂ conversion factors, α_{CO} . Our baseline calculation assumes an optically thick, thermalized gas $R_{4,1} \approx 1$ with $\alpha_{CO} = 0.8$, corresponding to local dusty starbursts and quasars. $R_{4,1} = 0.87$ is typically used for local quasars, and $R_{4,1} = 0.37$ corresponds to the calibration of IR-selected AGNs at cosmic noon (Kirkpatrick et al. 2019). We place an upper limit on M_{H_2} with $\alpha_{CO} = 3.2$, corresponding to main-sequence galaxies. The mean mass for the different relations is $\langle M_{H_2} \rangle = (6 \pm 5) \times 10^{10} M_{\odot}$.

	$R_{4,1} = 0.37 \pm 0.11$	$R_{4,1} = 0.87$	$R_{4,1} = 1$
$\alpha_{CO} = 0.8$	$(3.9 \pm 0.1) \times 10^{10} M_{\odot}$	$(1.8 \pm 0.1) \times 10^{10} M_{\odot}$	$(1.6 \pm 0.1) \times 10^{10} M_{\odot}$
$\alpha_{CO} = 3.2$	$(1.6 \pm 0.1) \times 10^{11} M_{\odot}$	$(7.1 \pm 0.5) \times 10^{10} M_{\odot}$	$(6.2 \pm 0.4) \times 10^{10} M_{\odot}$

is that the host galaxy environment of J0749+2255 has an extended starburst phase despite the depletion of the molecular gas reservoir (Chen et al. 2024). The high star formation efficiency is similar to hyperluminous quasars at cosmic noon (Bischetti et al. 2018). Although quasar-feedback is known to cause gas depletion (e.g. Bertola et al. 2024), fast gas outflows have not been detected in the molecular (this study) or ionized phases (JWST; Ishikawa et al. 2024). Thus, quasar feedback may be less impactful in J0749+2255 unlike some dual quasars seen by Tang et al. (2024). J0749+2255 provides evidence for enhanced star formation, concurrent with quasar activity, in a major gas-rich galaxy merger.

4.4. Synchrotron dominated continuum

The bright 455 GHz continuum is co-spatial with the bright radio sources seen in VLA (Chen et al. 2023b). In Figure 8, we map and plot the flux ratio values of the observed CO(4–3) and continuum, CO/continuum. We see a deficit of CO in the nuclei and an enhancement in the outskirts. This suggests that the nuclear component may dominate the observed continuum, which complicates the original goal of estimating the total far-infrared (FIR) luminosity to calculate SFR.

We also compare CO/continuum against the known L_{TIR} vs. CO ratio (Carilli & Walter 2013) in Figure 8. The caveat is that this is not a direct comparison since Carilli & Walter (2013) compares a galaxy’s global properties, whereas we can do this on a spaxel-by-spaxel basis within one object. Assuming that this relation is true at small spatial scales, < 1 kpc, we extrapolate the Carilli & Walter (2013) relation to lower L_{TIR} and L_{CO} values. It appears that the central regions have CO/continuum values that are at least comparable to or greater than starbursts, supporting the interpretation of enhanced star formation in J0749+2255.

We also examine the continuum emission in the context of the two quasars’ spectral energy distribution (SED). From the H α and PAH 3.3 μ m emission (Chen et al. 2024; Ishikawa et al. 2024), we know that J0749+2255 is hosted by an extreme starburst (SFR $> 1,000 M_{\odot} \text{ yr}^{-1}$). Since a quasar hosted by an extreme starburst is analogous to ultra-luminous

infrared galaxies (ULIRGs), we compare the SED of J0749+2255 with the template SED of ULIRGs (Rieke et al. 2009), scaled by the known SFR of J0749+2255. SFR is known to be correlated with the total infrared luminosity, L_{TIR} , summed over 8-1000 μ m. We estimate to be $L_{TIR} \approx 6 \times 10^{12} L_{\odot}$ using the Bell (2003) calibration. In Figure 9 we show the updated SED of J0749+2255 with the integrated continuum luminosity from Table 2. The SED also includes broadband photometric and spectroscopic data, including the most recent JWST NIRSpec and MIRI observations (Chen et al. 2022, 2023b, 2024; Ishikawa et al. 2024). We compare the observations with the quasar synchrotron power-law spectrum ($f_{\nu} \propto \nu^{-\alpha}$) extrapolated to 1 MHz, the model ULIRG starburst spectrum, a model Type 1 quasar FIR continuum (Lyu & Rieke 2017), and model radio-loud/quiet quasars (Shang et al. 2011). The starburst’s contribution to the radio and sub-mm is also negligible ($\sim 10^{41} \text{ erg s}^{-1}$ at 455 GHz). We see that neither the starburst nor the synchrotron model sufficiently explains the observed ALMA continuum. It appears that ALMA detects an excess sub-mm emission at 455 GHz.

The question of excess sub-mm- and mm-excess emission has been studied in radio-quiet quasars (e.g. Panessa et al. 2019; Hermelo et al. 2016). These systems typically have a flat or inverted synchrotron slope with an excess radio emission at higher frequencies. From Chen et al. (2023b), it is known that J0749+2255 is associated with two compact radio luminous cores with a loudness parameter of $R > 600$ and flat or inverted radio spectra. Likely explanations of the excess are optically thick (unlikely) synchrotron from a compact jet, magnetically heated corona from the inner-accretion disk, thermal free-free emission from the narrow line region or starburst activity or outflows (Panessa et al. 2022, and references therein).

Alternatively, the observed sub-mm continuum may arise from excess blackbody dust emission. We calculate the blackbody spectrum for cold dust with temperatures $T \approx 30$ K and $T \approx 45$ K, normalized by the SFR-predicted IR luminosity, $L_{TIR} \sim 10^{12} L_{\odot}$. We plot both spectra in Figure 9. This dust model assumes a

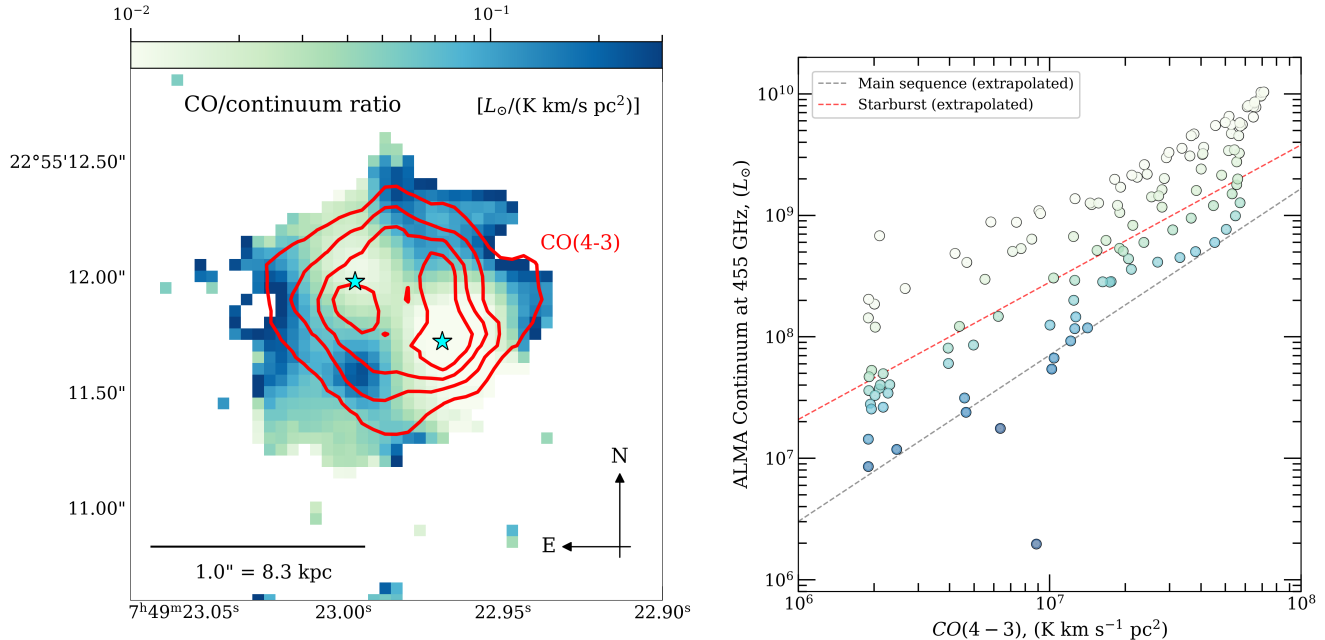


Figure 8. (Left) Map of the CO/continuum emission ratio. The red contours outline the clumpy structure of the CO emission at $\text{SNR} > 2$. We can see that the light-green regions, dominated by the nuclear synchrotron emission, have an elevated continuum despite the presence of CO(4 – 3), traced with the red contours. The outer regions of elevated CO, away from the continuum, in dark blue are likely dominated by star formation. (Right) The CO/continuum ratio separated by the differential spatial elements. The color shading matches the CO/continuum map. We compare to the known relations of local starburst and main-sequence galaxies (Carilli & Walter 2013 and references therein).

cold dust environment within a $r = 1.2$ kpc aperture around each quasar, despite potential heating from the luminous quasar radiation, intense starburst, and dynamical heating from merger activity. Also, there are no constraints on the dust properties; the two quasars are optically bright with no Balmer decrements detected (Chen et al. 2023b; Ishikawa et al. 2024). The combined contribution from the cold dust emission and the excess quasar synchrotron radiation may explain the observed 455 GHz continuum. However, this remains speculative without a constraint on the FIR and dust continuum.

4.5. Comparison and implication

The JWST (Chen et al. 2024; Ishikawa et al. 2024) and ALMA (this study) observations of J0749+2255 reveal a gas-rich host galaxy with intense star formation. The inferred Kennicutt-Schmidt relation of SFR vs. molecular mass showed that the molecular mass is lower than expected for the calculated SFR, suggesting an intense starburst rate exceeding the available fuel. The multi-phase gas kinematics are also complex. Although the ionized gas appears to suggest a single large rotating gas (Ishikawa et al. 2024), the CO kinematics reveals a dynamically disturbed environment, likely due to a merger, with two kinematically distinct structures.

If J0749+2255 is a result of a major galaxy merger, then the observed properties are similar to other known extreme starbursts like luminous infrared galaxies (LIRGs) and their extreme siblings, ultra-LIRGs (ULIRGs) and hyper-LIRG (HyLIRGs; Harrington et al. e.g. 2018; Liu et al. e.g. 2024) at cosmic noon. The SED fit shown in Figure 9 suggests that J0749+2255 has elevated mm-continuum not explained by starbursts, possibly due to additional contributions from the quasars. We can also see this trend in the CO/continuum ratio in Figure 8. The CO depletion suggested by the CO/continuum ratio is also consistent with luminous quasars at cosmic noon (Bischetti et al. 2018; Bertola et al. 2024), likely by extremely efficient star formation rather than quasar feedback. However, Tang et al. (2024) detected large molecular gas reservoirs in low redshift dual quasars.

Interestingly, studies of these extreme starbursts have also revealed rotating gas disks traced with CO emission (e.g. Downes & Solomon 1998). Assuming the presence of rotating CO gas, according to the kinematic decomposition in Section 3.3, then one interpretation is that J0749+2255 may be a superposition of two overlapping galaxies during an ongoing merger, either by

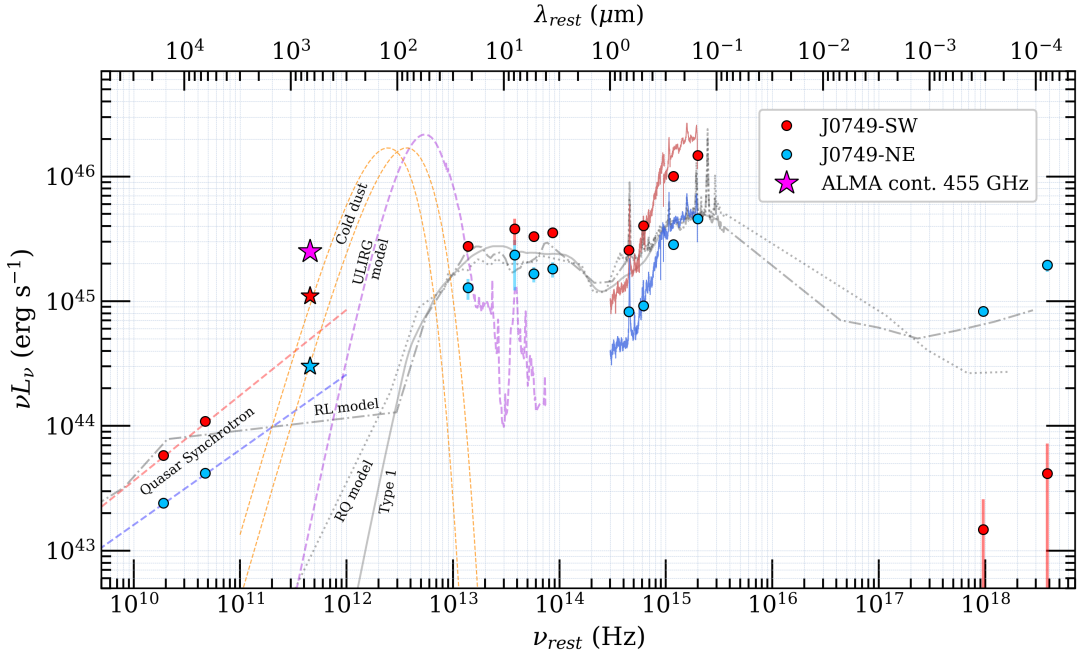


Figure 9. An updated SED of J0749+2255 adapted from Chen et al. (2023b, 2024) with the new ALMA measurements of the rest-frame 455 GHz continuum, optical and near-infrared spectroscopy (Ishikawa et al. 2024). The circles distinguish each quasar by color: J0749+2255-SW (red), J0749+2255-NE (blue), and integrated (purple). The radio-loud and radio-quiet SED models (grey dotted and dashed lines) are from the Shang et al. (2011) templates. The light purple dashed line shows the ULIRG template (Rieke et al. 2009; Bell 2003) calibrated to the known SFR. The radio/sub-mm luminosity converted from SFR is too small to be shown in this plot. The light red and blue dashed lines show the extrapolated synchrotron continuum. We also show two blackbody spectra assuming cold dust in dashed light orange.

chance alignment with the observer or in a close-passage. The detection of distinct kinematic gas components associated with each quasar may support this hypothesis. There is some evidence for this, possibly among low redshift dual quasars. Koss et al. (2023) detected distinct 231 GHz continuum cores and a velocity differential in the CO(2-1) emission, which serves as evidence for two kinematically independent nuclei in Mrk 463 at $z = 0.005355$. Mrk 739, a $z = 0.02985$ dual quasar with ~ 3.4 kpc is more kinematically ambiguous and has been interpreted with the overlapping-galaxy model (Koss et al. 2011; Tubín et al. 2021). There are indications from simulations that dual quasars at $z \sim 2$ are most likely hosted by disk host galaxies (Dadiani et al. 2024). The other interpretation of J0749+2255 is that it is undergoing a violent merger. Kinematic analysis of CO(2-1) by Tang et al. (2024) reveals that their sample of local dual quasars ($z \approx 0.5$) are merger-like, yet ambiguities with the rotation interpretation remain. Clearly, these studies have the advantage of proximity that enables detailed studies of dual quasars.

These comparisons suggest that dual quasars have distinct properties from starbursts, although the exact cause is not yet clear. According to the case study of

J0749+2255, it would seem that mergers may fuel and trigger intense star formation. However, the connection with the quasar activity remains unclear, nor is there a consensus in the literature. Tang et al. (2024) showed that local dual quasars have no obvious correlation between the molecular properties and quasar separation. Quasar feedback was implied in some dual quasars (e.g. Izumi et al. 2024; Tang et al. 2024; Ruby et al. 2024); however, J0749+2255 appears to show little evidence for quasar feedback. While J0749+2255 may be an outlier, it appears that merger connection with quasar feedback remains an open question. A more robust sample comparing the host galaxies of dual quasars (e.g., SFR, dynamics, gas content) and galaxy mergers is needed to fully address the role of galaxy mergers on quasars and galaxy evolution.

5. SUMMARY AND CONCLUSION

We observed a $z = 2.17$ dual quasar, J0749+2255, with ALMA Band 4 to detect the molecular gas and the underlying component. We detect the CO(4-3) $\lambda 650\mu\text{m}$ emission at 145.434 GHz and the nearby continuum at 143.538 GHz or at rest-frame 455 GHz.

We find that the CO(4-3) emission has a kinematically and morphologically complex structure. Over-

all, the single-component CO(4 – 3) line fits indicates that the v_{50} velocity map is similar to that of the ionized gas seen with H α (Ishikawa et al. 2024) with a red-/blue-shifted velocity gradient. From the detailed global line fits, we find that the CO gas can be separated into two distinct kinematic components: a narrow line ($w_{80} \sim 150 \text{ km s}^{-1}$) component and a broad line ($w_{80} \sim 320 \text{ km s}^{-1}$) component.

The CO kinematics provides compelling evidence to mark a significant step forward in the lensing debate surrounding J0749+2255. Kinematic analyses contradict the predictions from the lensing hypothesis supporting the dual quasar interpretation the spectral dis-similarity of the CO emission (Figure 4) and an extended CO that is morphologically and kinematically complex that eliminates the lens-like CO ring (Figures 5 and 6). The CO ring initially shown in the integrated intensity map is likely an artifact due to the blending of the kinematically distinct emission line components. Thus, we argue that J0749+2255 is indeed a dual quasar.

We examine the v_{50}/σ ratio of the narrow line and broad line gas components to assess the dynamical state of the CO gas. The v_{50}/σ maps suggest that the CO gas in J0749+2255 is kinematically disturbed with two distinct dynamical phases: a dynamically complex, slow-moving gas and a turbulent, fast-moving gas. The CO kinematics suggest that J0749+2255 is likely undergoing a galaxy merger event. However, some ambiguities remain in the exact kinematic interpretation of each component. This interpretation contradicts the gas rotation seen in the ionized gas phase (Ishikawa et al. 2024). It may be possible that the ionized and molecular gas phases trace different dynamics.

We calculate a total molecular mass of $M_{H_2} = (6 \pm 5) \times 10^{10} M_{\odot}$, in which the uncertainty is dominated by the different choice of conversion factors. If we compare the known SFR ($\sim 1000 M_{\odot} \text{ yr}^{-1}$) with M_{H_2} , we find that the ratio is above the Kennicutt-Schmidt relation for main-sequence galaxies (Kennicutt 1998). This suggests that the host galaxy environment of J0749+2255 is undergoing rapid star formation that exceeds the available fuel, possibly driven by the merger dynamics. Since no quasar-driven outflows have been detected, it is unlikely that the CO depletion is driven by quasar feedback.

The rest-frame 455 GHz continuum is mostly dominated by the two compact cores that are co-spatial with the quasars. There is also an extended continuum component, stretching asymmetrically to the southwest by nearly 8 kpc. The L_{CO}/L_{cont} ratio shows that the nu-

clear regions of the quasars are dominated by the continuum emission, whereas the CO(4 – 3) emission dominates in the outskirts. The CO/continuum ratio and the SFR/ M_{H_2} ratio (from Chen et al. 2024) indicate possible CO depletion. Interestingly, the nuclear 455 GHz continuum cannot be explained by an extreme starburst model or by the extrapolated synchrotron emission. Instead, the observed continuum may be associated with the excess emission from nuclear synchrotron radiation and possibly cold dust, whereas the outskirts are likely dominated by star formation.

This study, combined with previous JWST observations, demonstrates the power of spatially-resolved spectroscopy in significantly advancing our understanding of dual quasars. Although ambiguities in the kinematic interpretation remain, ALMA provides evidence of complex kinematics supporting the merger interpretation. Future observations of the stellar continuum and higher angular resolution may help address the ambiguity. The merger activity may fuel the intense starburst activity in J0749+2255 and the two quasars. However, it is unclear whether this behavior is representative of the dual quasar population or if J0749+2255 is an outlier. Detailed statistical studies is needed to address the mechanisms of dual quasars and the merger-quasar connection.

1 The National Radio Astronomy Observatory is a facil-
 2 ity of the National Science Foundation operated un-
 3 der cooperative agreement by Associated Universities,
 4 Inc. This paper makes use of the following ALMA
 5 data: ADS/JAO.ALMA#2022.1.01427.S. ALMA is a
 6 partnership of ESO (representing its member states),
 7 NSF (USA) and NINS (Japan), together with NRC
 8 (Canada), MOST and ASIAA (Taiwan), and KASI (Re-
 9 public of Korea), in cooperation with the Republic of
 10 Chile. The Joint ALMA Observatory is operated by
 11 ESO, AUI/NRAO and NAOJ.

12 Y.I. acknowledges support from the Space@Hopkins
 13 Graduate Fellowship. Y.I., N.L.Z., Y.-C.C., A.V., H.-
 14 C.H., and S.S. were supported in part by JWST-GO-
 15 02654 grant by the Space Telescope Science Institute.
 16 Y.S. and X.L. acknowledge support by NSF grant AST-
 17 2108162. Y.I. thanks D. Coe, T. Heckman, D. Neufeld,
 18 C. Norman, M. Onoue, J. Silverman, and M. Yue for
 19 useful discussions.

Facilities: ALMA

Software: `astropy` (Astropy Collaboration et al. 2013, 2018, 2022), `CASA` (The CASA Team et al. 2022)

REFERENCES

- Accurso, G., Saintonge, A., Catinella, B., et al. 2017, MNRAS, 470, 4750, doi: [10.1093/mnras/stx1556](https://doi.org/10.1093/mnras/stx1556)
- Agnello, A., Grillo, C., Jones, T., et al. 2018, MNRAS, 474, 3391, doi: [10.1093/mnras/stx2950](https://doi.org/10.1093/mnras/stx2950)

- Aihara, H., Arimoto, N., Armstrong, R., et al. 2018, PASJ, 70, S4, doi: [10.1093/pasj/psx066](https://doi.org/10.1093/pasj/psx066)
- Astropy Collaboration, Robitaille, T. P., Tollerud, E. J., et al. 2013, A&A, 558, A33, doi: [10.1051/0004-6361/201322068](https://doi.org/10.1051/0004-6361/201322068)
- Astropy Collaboration, Price-Whelan, A. M., Sipőcz, B. M., et al. 2018, AJ, 156, 123, doi: [10.3847/1538-3881/aabc4f](https://doi.org/10.3847/1538-3881/aabc4f)
- Astropy Collaboration, Price-Whelan, A. M., Lim, P. L., et al. 2022, ApJ, 935, 167, doi: [10.3847/1538-4357/ac7c74](https://doi.org/10.3847/1538-4357/ac7c74)
- Banerji, M., Carilli, C. L., Jones, G., et al. 2017, MNRAS, 465, 4390, doi: [10.1093/mnras/stw3019](https://doi.org/10.1093/mnras/stw3019)
- Begelman, M., Blandford, R., & Rees, M. 1980, Nature, 287, 307, doi: [10.1038/287307a0](https://doi.org/10.1038/287307a0)
- Bell, E. F. 2003, ApJ, 586, 794, doi: [10.1086/367829](https://doi.org/10.1086/367829)
- Bertola, E., Circosta, C., Ginolfi, M., et al. 2024, A&A, 691, A178, doi: [10.1051/0004-6361/202450420](https://doi.org/10.1051/0004-6361/202450420)
- Bischetti, M., Piconcelli, E., Vietri, G., et al. 2017, A&A, 598, A122, doi: [10.1051/0004-6361/201629301](https://doi.org/10.1051/0004-6361/201629301)
- Bischetti, M., Piconcelli, E., Feruglio, C., et al. 2018, A&A, 617, A82, doi: [10.1051/0004-6361/201833249](https://doi.org/10.1051/0004-6361/201833249)
- Bischetti, M., Feruglio, C., Piconcelli, E., et al. 2021, A&A, 645, A33, doi: [10.1051/0004-6361/202039057](https://doi.org/10.1051/0004-6361/202039057)
- Blaes, O., Lee, M. H., & Socrates, A. 2002, ApJ, 578, 775, doi: [10.1086/342655](https://doi.org/10.1086/342655)
- Bolatto, A. D., Wolfire, M., & Leroy, A. K. 2013, ARA&A, 51, 207, doi: [10.1146/annurev-astro-082812-140944](https://doi.org/10.1146/annurev-astro-082812-140944)
- Brusa, M., Cresci, G., Daddi, E., et al. 2018, A&A, 612, A29, doi: [10.1051/0004-6361/201731641](https://doi.org/10.1051/0004-6361/201731641)
- Carilli, C., & Walter, F. 2013, ARA&A, 51, 105, doi: [10.1146/annurev-astro-082812-140953](https://doi.org/10.1146/annurev-astro-082812-140953)
- Chen, N., Matteo, T. D., Ni, Y., et al. 2023a, MNRAS, 522, 1895, doi: [10.1093/mnras/stad834](https://doi.org/10.1093/mnras/stad834)
- Chen, Y.-C., Hwang, H.-C., Shen, Y., et al. 2022, ApJ, 925, 162, doi: [10.3847/1538-4357/ac401b](https://doi.org/10.3847/1538-4357/ac401b)
- Chen, Y.-C., Liu, X., Foord, A., et al. 2023b, Nature, 616, 45, doi: [10.1038/s41586-023-05766-6](https://doi.org/10.1038/s41586-023-05766-6)
- Chen, Y.-C., Ishikawa, Y., Zakamska, N. L., et al. 2024, ApJ, 968, 92, doi: [10.3847/1538-4357/ad4798](https://doi.org/10.3847/1538-4357/ad4798)
- Ciurlo, A., Mannucci, F., Yeh, S., et al. 2023, A&A, 671, L4, doi: [10.1051/0004-6361/202345853](https://doi.org/10.1051/0004-6361/202345853)
- Dadiani, E., Matteo, T. D., Chen, N., et al. 2024, The Open Journal of Astrophysics, 7, 84, doi: [10.33232/001c.124451](https://doi.org/10.33232/001c.124451)
- Díaz-Santos, T., Assef, R. J., Blain, A. W., et al. 2016, ApJL, 816, L6, doi: [10.3847/2041-8205/816/1/L6](https://doi.org/10.3847/2041-8205/816/1/L6)
- Downes, D., & Solomon, P. M. 1998, ApJ, 507, 615, doi: [10.1086/306339](https://doi.org/10.1086/306339)
- Duras, F., Bongiorno, A., Piconcelli, E., et al. 2017, A&A, 604, A67, doi: [10.1051/0004-6361/201731052](https://doi.org/10.1051/0004-6361/201731052)
- Elbaz, D., Daddi, E., Le Borgne, D., et al. 2007, A&A, 468, 33, doi: [10.1051/0004-6361:20077525](https://doi.org/10.1051/0004-6361:20077525)
- Fan, L., Knudsen, K. K., Han, Y., & Tan, Q.-h. 2019, ApJ, 887, 74, doi: [10.3847/1538-4357/ab5059](https://doi.org/10.3847/1538-4357/ab5059)
- Feruglio, C., Fiore, F., Carniani, S., et al. 2018, A&A, 619, A39, doi: [10.1051/0004-6361/201833174](https://doi.org/10.1051/0004-6361/201833174)
- Gross, A. C., Chen, Y.-C., Foord, A., et al. 2023, ApJ, 956, 117, doi: [10.3847/1538-4357/acf469](https://doi.org/10.3847/1538-4357/acf469)
- Harrington, K. C., Yun, M. S., Magnelli, B., et al. 2018, MNRAS, 474, 3866, doi: [10.1093/mnras/stx3043](https://doi.org/10.1093/mnras/stx3043)
- Hawkins, M. R. S., Clements, D., Fried, J. W., et al. 1997, MNRAS, 291, 811, doi: [10.1093/mnras/291.4.811](https://doi.org/10.1093/mnras/291.4.811)
- He, H., Bottrell, C., Wilson, C., et al. 2023, ApJ, 950, 56, doi: [10.3847/1538-4357/acca76](https://doi.org/10.3847/1538-4357/acca76)
- Heckman, T. M., & Best, P. N. 2014, ARA&A, 52, 589, doi: [10.1146/annurev-astro-081913-035722](https://doi.org/10.1146/annurev-astro-081913-035722)
- Hermelo, I., Relaño, M., Lisenfeld, U., et al. 2016, A&A, 590, A56, doi: [10.1051/0004-6361/201525816](https://doi.org/10.1051/0004-6361/201525816)
- Herrera-Camus, R., Tacconi, L., Genzel, R., et al. 2019, ApJ, 871, 37, doi: [10.3847/1538-4357/aaf6a7](https://doi.org/10.3847/1538-4357/aaf6a7)
- Hopkins, P. F., & Hernquist, L. 2009, ApJ, 694, 599, doi: [10.1088/0004-637X/694/1/599](https://doi.org/10.1088/0004-637X/694/1/599)
- Hwang, H.-C., Shen, Y., Zakamska, N., & Liu, X. 2020, ApJ, 888, 73, doi: [10.3847/1538-4357/ab5c1a](https://doi.org/10.3847/1538-4357/ab5c1a)
- Ishikawa, Y., Zakamska, N. L., Shen, Y., et al. 2024, arXiv e-prints, arXiv:2403.08098, <http://arxiv.org/abs/2403.08098>
- Izumi, T., Matsuoka, Y., Onoue, M., et al. 2024, ApJ, 972, 116, doi: [10.3847/1538-4357/ad57c6](https://doi.org/10.3847/1538-4357/ad57c6)
- Kakkad, D., Mainieri, V., Brusa, M., et al. 2017, MNRAS, 468, 4205, doi: [10.1093/mnras/stx726](https://doi.org/10.1093/mnras/stx726)
- Kennicutt, R. C. 1998, ARA&A, 36, 189, doi: [10.1146/annurev.astro.36.1.189](https://doi.org/10.1146/annurev.astro.36.1.189)
- Kirkpatrick, A., Sharon, C., Keller, E., & Pope, A. 2019, ApJ, 879, 41, doi: [10.3847/1538-4357/ab223a](https://doi.org/10.3847/1538-4357/ab223a)
- Koss, M., Mushotzky, R., Veilleux, S., et al. 2011, ApJ, 735, L42, doi: [10.1088/2041-8205/735/2/L42](https://doi.org/10.1088/2041-8205/735/2/L42)
- Koss, M. J., Blecha, L., Bernhard, P., et al. 2018, Nature, 563, 214, doi: [10.1038/s41586-018-0652-7](https://doi.org/10.1038/s41586-018-0652-7)
- Koss, M. J., Treister, E., Kakkad, D., et al. 2023, ApJL, 942, L24, doi: [10.3847/2041-8213/aca8f0](https://doi.org/10.3847/2041-8213/aca8f0)
- Lamperti, I., Harrison, C. M., Mainieri, V., et al. 2021, A&A, 654, A90, doi: [10.1051/0004-6361/202141363](https://doi.org/10.1051/0004-6361/202141363)
- Liu, D., Schreiber, N. M. F., Harrington, K. C., et al. 2024, Nature Astronomy, doi: [10.1038/s41550-024-02296-7](https://doi.org/10.1038/s41550-024-02296-7)
- Lyu, J., & Rieke, G. H. 2017, ApJ, 841, 76, doi: [10.3847/1538-4357/aa7051](https://doi.org/10.3847/1538-4357/aa7051)
- Maiolino, R., Gallerani, S., Neri, R., et al. 2012, MNRAS, 425, L66, doi: [10.1111/j.1745-3933.2012.01303.x](https://doi.org/10.1111/j.1745-3933.2012.01303.x)
- Mannucci, F., Pancino, E., Belfiore, F., et al. 2022, Nature Astronomy, 6, 1185, doi: [10.1038/s41550-022-01761-5](https://doi.org/10.1038/s41550-022-01761-5)

- Matteo, T. D., Springel, V., & Hernquist, L. 2005, *Nature*, 433, 604, doi: [10.1038/nature03335](https://doi.org/10.1038/nature03335)
- Mazzilli Ciraulo, B., Melchior, A.-L., Maschmann, D., et al. 2021, *A&A*, 653, A47, doi: [10.1051/0004-6361/202141319](https://doi.org/10.1051/0004-6361/202141319)
- Mechtley, M., Jahnke, K., Windhorst, R., et al. 2016, *ApJ*, 830, 156, doi: [10.3847/0004-637X/830/2/156](https://doi.org/10.3847/0004-637X/830/2/156)
- Milosavljević, M., & Merritt, D. 2001, *ApJ*, 563, 34, doi: [10.1086/323830](https://doi.org/10.1086/323830)
- Nguyen, N. H., Lira, P., Trakhtenbrot, B., et al. 2020, *ApJ*, 895, 74, doi: [10.3847/1538-4357/ab8bd3](https://doi.org/10.3847/1538-4357/ab8bd3)
- Noeske, K. G., Weiner, B. J., Faber, S. M., et al. 2007, *ApJL*, 660, L43, doi: [10.1086/517926](https://doi.org/10.1086/517926)
- Panessa, F., Baldi, R. D., Laor, A., et al. 2019, *Nature Astronomy*, 3, 387, doi: [10.1038/s41550-019-0765-4](https://doi.org/10.1038/s41550-019-0765-4)
- Panessa, F., Chiaraluce, E., Bruni, G., et al. 2022, *MNRAS*, 515, 473, doi: [10.1093/mnras/stac1745](https://doi.org/10.1093/mnras/stac1745)
- Papadopoulos, P. P., Werf, P. v. d., Xilouris, E., Isaak, K. G., & Gao, Y. 2012, *ApJ*, 751, 10, doi: [10.1088/0004-637X/751/1/10](https://doi.org/10.1088/0004-637X/751/1/10)
- Perna, M., Arribas, S., Marshall, M., et al. 2023, *A&A*, 679, A89, doi: [10.1051/0004-6361/202346649](https://doi.org/10.1051/0004-6361/202346649)
- Prusti, T., Bruijne, J. H. J. d., Brown, A. G. A., et al. 2016, *A&A*, 595, A1, doi: [10.1051/0004-6361/201629272](https://doi.org/10.1051/0004-6361/201629272)
- Riechers, D. A., Walter, F., Brewer, B. J., et al. 2008, *ApJ*, 686, 851, doi: [10.1086/591434](https://doi.org/10.1086/591434)
- Rieke, G. H., Alonso-Herrero, A., Weiner, B. J., et al. 2009, *ApJ*, 692, 556, doi: [10.1088/0004-637X/692/1/556](https://doi.org/10.1088/0004-637X/692/1/556)
- Rizzo, F., Roman-Oliveira, F., Fraternali, F., et al. 2023, *A&A*, 679, A129, doi: [10.1051/0004-6361/202346444](https://doi.org/10.1051/0004-6361/202346444)
- Ruby, M., Müller-Sánchez, F., Comerford, J. M., et al. 2024, *MNRAS*, 535, 763, doi: [10.1093/mnras/stae2320](https://doi.org/10.1093/mnras/stae2320)
- Schneider, D. P., Richards, G. T., Hall, P. B., et al. 2010, *AJ*, 139, 2360, doi: [10.1088/0004-6256/139/6/2360](https://doi.org/10.1088/0004-6256/139/6/2360)
- Scialpi, M., Mannucci, F., Marconcini, C., et al. 2024, *A&A*, 690, A57, doi: [10.1051/0004-6361/202347242](https://doi.org/10.1051/0004-6361/202347242)
- Shang, Z., Brotherton, M. S., Wills, B. J., et al. 2011, *ApJS*, 196, 2, doi: [10.1088/0067-0049/196/1/2](https://doi.org/10.1088/0067-0049/196/1/2)
- Shen, Y., Hall, P. B., Horne, K., et al. 2019, *ApJS*, 241, 34, doi: [10.3847/1538-4365/ab074f](https://doi.org/10.3847/1538-4365/ab074f)
- Shen, Y., Chen, Y.-C., Hwang, H.-C., et al. 2021, *Nature Astronomy*, 5, 569, doi: [10.1038/s41550-021-01323-1](https://doi.org/10.1038/s41550-021-01323-1)
- Silk, J., & Rees, M. J. 1998, *A&A*, 331, L1, <http://arxiv.org/abs/astro-ph/9801013>
- Sluse, D., Hutsemékers, D., Courbin, F., Meylan, G., & Wambsganss, J. 2012, *A&A*, 544, A62, doi: [10.1051/0004-6361/201219125](https://doi.org/10.1051/0004-6361/201219125)
- Solomon, P. M., & Vanden Bout, P. A. 2005, *ARA&A*, 43, 677, doi: [10.1146/annurev.astro.43.051804.102221](https://doi.org/10.1146/annurev.astro.43.051804.102221)
- Stacey, H. R., Costa, T., McKean, J. P., et al. 2022, *MNRAS*, 517, 3377, doi: [10.1093/mnras/stac2765](https://doi.org/10.1093/mnras/stac2765)
- Stacey, H. R., & McKean, J. P. 2018, *Monthly Notices of the Royal Astronomical Society: Letters*, 481, L40, doi: [10.1093/mnrasl/sly153](https://doi.org/10.1093/mnrasl/sly153)
- Stuber, S. K., Schinnerer, E., Williams, T. G., et al. 2023, *A&A*, 676, A113, doi: [10.1051/0004-6361/202346318](https://doi.org/10.1051/0004-6361/202346318)
- Tacconi, L. J., Genzel, R., Smail, I., et al. 2008, *ApJ*, 680, 246, doi: [10.1086/587168](https://doi.org/10.1086/587168)
- Tang, S., Silverman, J. D., Liu, Z., et al. 2024, *arXiv e-prints*, arXiv:2407.09399, doi: [10.48550/arXiv.2407.09399](https://doi.org/10.48550/arXiv.2407.09399)
- The CASA Team, Bean, B., Bhatnagar, S., et al. 2022, *PASP*, 134, 114501, doi: [10.1088/1538-3873/ac9642](https://doi.org/10.1088/1538-3873/ac9642)
- Trakhtenbrot, B., Lira, P., Netzer, H., et al. 2017, *ApJ*, 836, 8, doi: [10.3847/1538-4357/836/1/8](https://doi.org/10.3847/1538-4357/836/1/8)
- Treister, E., Privon, G. C., Sartori, L. F., et al. 2018, *ApJ*, 854, 83, doi: [10.3847/1538-4357/aaa963](https://doi.org/10.3847/1538-4357/aaa963)
- Tubín, D., Treister, E., D'Ago, G., et al. 2021, *ApJ*, 911, 100, doi: [10.3847/1538-4357/abedba](https://doi.org/10.3847/1538-4357/abedba)
- Valentino, F., Daddi, E., Puglisi, A., et al. 2021, *A&A*, 654, A165, doi: [10.1051/0004-6361/202141417](https://doi.org/10.1051/0004-6361/202141417)
- Vayner, A., Zakamska, N., Wright, S. A., et al. 2021, *ApJ*, 923, 59, doi: [10.3847/1538-4357/ac2b9e](https://doi.org/10.3847/1538-4357/ac2b9e)
- Wisnioski, E., Schreiber, N. M. F., Wuyts, S., et al. 2015, *ApJ*, 799, 209, doi: [10.1088/0004-637X/799/2/209](https://doi.org/10.1088/0004-637X/799/2/209)
- Xie, Y., Ho, L. C., Zhuang, M.-Y., & Shangguan, J. 2021, *ApJ*, 910, 124, doi: [10.3847/1538-4357/abe404](https://doi.org/10.3847/1538-4357/abe404)
- Yu, Q. 2002, *MNRAS*, 331, 935, doi: [10.1046/j.1365-8711.2002.05242.x](https://doi.org/10.1046/j.1365-8711.2002.05242.x)
- Zakamska, N. L., & Greene, J. E. 2014, *MNRAS*, 442, 784, doi: [10.1093/mnras/stu842](https://doi.org/10.1093/mnras/stu842)